J. Fluid Mech. (1989), *vol.* 199, *pp.* 177–215
Printed in Great Britain

The motion of a finite mass of granular material down a rough incline

By S. B. SAVAGE† AND K. HUTTER‡
Laboratory of Hydraulics, Hydrology and Glaciology, Swiss Federal Institute of Technology, Zürich

(Received 24 October 1986 and in revised from 21 May 1988)

Rock, snow and ice masses are often dislodged on steep slopes of mountainous regions. The masses, which typically are in the form of innumerable discrete blocks or granules, initially accelerate down the slope until the angle of inclination of the bed approaches the horizontal and bed friction eventually brings them to rest. The present paper describes an initial investigation which considers the idealized problem of a finite mass of material released from rest on a rough inclined plane. The granular mass is treated as a frictional Coulomb-like continuum with a Coulomb-like basal friction law. Depth-averaged equations of motion are derived; they bear a superficial resemblance to the nonlinear shallow-water wave equations. Two similarity solutions are found for the motion. They both are of surprisingly simple analytical form and show a rather unanticipated behaviour. One has the form of a pile of granular material in the shape of a parabolic cap and the other has the form of an M-wave with vertical faces at the leading and trailing edges. The linear stability of the similarity solutions is studied. A restricted stability analysis, in which the spread is left unperturbed shows them to be stable, suggesting that mathematically both are possible asymptotic wave forms. Two numerical finite-difference schemes, one of Lagrangian, the other of Eulerian type, are presented. While the Eulerian technique is able to reproduce the M-wave similarity solution, it appears to give spurious results for more general initial conditions and the Lagrangian technique is best suited for the present problem. The numerical predictions are compared with laboratory experiments of Huber (1980) involving the motion of gravel released from rest on a rough inclined plane. Although in these experiments the continuum approximation breaks down at large times when the gravel layer is only a few particle diameters thick, the general features of the development of the gravel mass are well predicted by the numerical solutions.

1. Introduction

Landslides, rockfalls and snow and ice avalanches that initiate on steep slopes can travel large distances before they come to rest. Their occurrence is largely unpredictable, and in mountainous regions like the Alps they often constitute a threat both to human life and property. Prominent examples are the Elm rockfall (Switzerland) in 1881 (Heim 1882, 1932; Hsü 1978), the Sherman Glacier rock avalanche (Alaska) in 1964 (Shreve 1966, 1968*a*; McSaveney 1978), the prehistoric Blackhawk landslide (Alaska) (Shreve 1968*b*) and the various ice avalanches resulting from large ice masses breaking off from Bisgletscher at Weisshorn

† Permanent address: Department of Civil Engineering and Applied Mechanics, McGill University, Montreal, Canada.
‡ Permanent address: Department of Mechanics, Technological Institute, Darmstadt, West Germany.

(Switzerland) in 1636, 1819 and 1973 (Roethlisberger 1978, 1981) and from Alalingletscher (Switzerland) in 1965 (Roethlisberger 1974, 1978). In addition, there are hundreds of smaller ice and snow avalanches that occur each year in Switzerland alone and cause numerous casualties (Alean 1984, 1985; Salm 1966; Perla & Martinelli 1978).

It has been observed that the slide behaves in a near fluid-like manner in that the granular material can be deposited in a very long and thin layer such that the nose moves through a surprisingly long distance. It has been suggested that the runout distance is volume dependent (Scheidegger 1975; Davies 1982); the larger the volume the larger the relative runout distance. Hypotheses to explain the fluidization have also been proposed (Erismann 1986; Goguel 1978; Hsü 1975; Kent 1965; Shreve 1968*a*). The essence of each of these hypotheses is to introduce some novel type of fluidization mechanism to produce the high mobility of the large-volume rockfalls. Upward flow of air, hovercraft action, generation of high-pressure steam, lubrication by molten rock and the development of a thin rapidly shearing layer of vigorously fluctuating particles beneath a densely packed overburden are among the suggested mechanisms. Except for the last (Dent 1986; Hutter, Szidarovszky & Yakowitz 1986), none of these proposals has been accompanied by either a rough or detailed computation of the flow development.

Direct observations of the dynamics of rockfalls or avalanches are extremely difficult to make and are possible only by remote sensing techniques. Gubler (1987), using radar Doppler techniques, has been successful in following a few artificially released snow flow avalanches, but we know of no measurements of the dynamics of large masses of rocks or soil. Laboratory experiments of dry gravel flow have been conducted by Huber (1980) to predict the surface water waves in lakes due to rockfalls plunging into the water. The part of his experiments dealing with gravel flow is detailed enough to permit the description of the temporal evolution of the front and rear edges of the moving gravel down a plane surface. It is only recently that Plüss (1987) and Hutter, Plüss & Maeno (1988) have performed additional experiments along curved beds. Their chute contains a straight inclined portion. To date, these experiments are probably the only ones against which a theoretical model of the motion of a finite mass of gravel down an incline can be tested.

This study is concerned with the development of a simple model for the flow and spreading of a finite volume of cohesionless granular material released from rest on rough inclines. The granular material is treated as an incompressible Coulomb continuum. Since we permit sliding to take place along the bed, a basal friction law is the second phenomenological relation that must be imposed on our model. As is customary, a dry Coulomb-like friction law is used for it; it relates the shear traction to the normal pressure at the base and involves the friction angle between the gravel and the rough bed.

In §2 we present the model and simplify it by introducing a scaling analysis that takes explicit account of the fact that the moving gravel masses are long and shallow. This shallowness and/or long-wave assumption manifests itself in the hydrostatic pressure relation. Depth averaging the equations of conservation of mass and momentum leads to evolution equations for the profile geometry and transport (average longitudinal velocity) reminiscent of the nonlinear shallow-water equations.

A fixed-domain mapping introduced in §3 transforms these equations to a simpler form; from these new equations two similarity solutions with surprisingly simple analytical structure are constructed. One of these solutions has a parabolic cap profile; in the asymptotic limit as $t \to \infty$ its width spreads linearly in time and its

height decreases as t^{-1}. The second solution has cliff-like edges and smaller depths towards the middle of the moving mass; it will be referred to as an M-wave. Its spread grows as $t^{\frac{2}{3}}$ and its height decreases as $t^{-\frac{2}{3}}$ when $t \to \infty$. Thus, for large time the asymptotic spread of the M-wave is smaller and the decrease in height is slower than for the parabolic cap profile.

The linearized stability analysis in §4 shows rigorously that the parabolic cap and the M-wave solutions are stable against small perturbations which leave the spread of the moving mass unperturbed. We have not been able to construct general stability statements, but the limited analysis performed for the two solutions makes their stability probable.

The equations of motion for the profile geometry and the transport have also been numerically integrated by finite-difference techniques (§5). The difficulties in finding a numerically accurate and stable finite difference scheme are noted. Two numerical schemes are presented, one Eulerian, the other Lagrangian. The former is able to reproduce the motion of the M-wave similarity solution quite well. On the other hand, it appears that even when the initial profile is something other than an M-wave, say the parabolic cap shape, the Eulerian numerical scheme eventually forces the profile into the M-wave solution. Such behaviour was not apparent in the laboratory experiments and it appears to be a numerical aberration. A second Lagrangian approach in which the grid is advected with the material particles is a natural choice for this problem which involves the determination of an unknown interface corresponding to the upper free surface of the finite mass of granular material.

Section 6, finally, presents a comparison of our numerical predictions with a selection of laboratory experiments of Huber (1980) involving the motion of gravel released from rest on a rough inclined plane. Comparison with these experimental data clearly indicates that the gravel flow selects asymptotically the parabolic similarity solution. Considering that (i) initial configurations of the gravel mass in the experiments could not be accurately reproduced in the computations and (ii) the continuum model is doubtful in these experiments at larger times because the gravel layer is only a few particle diameters thick, the general features of the gravel mass dispersion are well predicted by the numerical solutions.

These results suggest that the present model can be used for the prediction of the motion of landslides, rockfalls, ice and snow (flow) avalanches. Extensions are presently underway to apply it to flows on more realistic beds which are curved and approach a horizontal flat.

2. Governing equations

We shall precede the detailed derivation of the governing equations by a physical discussion to provide a motivation and justification for what might appear at first glance to be some rather sweeping simplifying assumptions.

2.1. *Discussion of major assumptions*

2.1.1 *Experimental evidence concerning rate-dependence of bed friction angle*

Previous studies of the behaviour of granular materials have often dealt with one or the other of two main characterizations (see Savage 1984). The earlier one (based upon soil mechanics work) which was usually meant for quasi-static deformations, shows no rate-dependence, and relates the shear stress at some point on a plane element to the shear stress there through the Mohr–Coulomb yield criterion. Some of

the more recent studies including kinetic theories of granular flows (for example, Jenkins & Savage 1983; Haff 1983; Lun *et al.* 1984; Jenkins & Richman 1985; Campbell & Gong 1986; and Walton & Braun 1986) and annular-shear-cell experiments (Savage & Sayed 1984; Hanes & Inman 1985) have considered the other characterization for the rapid flow regime. They have examined the rate-dependence in detail and found that for constant bulk solids concentration the stresses depend approximately upon the square of the shear rate, a very strong rate-dependence indeed. The same rate-dependent mechanisms are at work at the boundaries. As a consequence one might infer that it is essential that constitutive models of the granular material both in the interior as well as at the basal boundaries exhibit significant rate dependence. As paradoxical as it may seem, the constitutive assumption used in the analysis of the present paper does not explicitly include any rate effects, but it is based upon an approximation of the experimental behaviour which has been observed by several investigators. Through the use of depth-averaged equations of motion we can exploit the simplicity which is inherent in these observations.

The depth averaging to be performed in the present paper will yield a momentum equation that contains the shear stress at the bed. We thus require suitable constitutive assumptions which describe the velocity dependence of this bed shear stress. We shall begin with a brief physical discussion of the dominant effects in different flow regimes, mention some previous constitutive proposals, and then attempt to summarize the available laboratory experimental evidence from shear cell tests and free-surface open channel flows to give some support for the constitutive assumptions to be used in the present work. Attention will be focused upon results of tests which have particular relevance to the avalanche flow under consideration.

Let us consider how the bed shear stress for a layer of cohesionless granular material of uniform thickness flowing over a rough bottom varies with flow rate. We also assume that the bed normal stress remains fixed; thus, a reduction in bulk density that might result (at high shear-rates) from an increase in flow velocity is accompanied by an associated expansion of the layer of granular material, keeping the bed normal stress (which is due to the weight of the overburden) constant.

At very slow shear rates the interparticle contacts are relatively slowly changing and particle inertia effects are negligible. The bed shear stress is due to the resultant integrated normal and tangential (dry frictional) forces at the particle contact points. One finds a quasi-static, rate-independent behaviour that can be well described by a Coulomb yield criterion.

At the other extreme at high shear rates, and at moderate solids concentrations, the particles acquire vigorous fluctuating motions in addition to their mean transport motion and interparticle contacts are short-lived. The stresses and other transport properties result from kinetic and collisional transfer of momentum, mass, energy, etc. This flow regime has been analysed by the previously mentioned kinetic theories of granular flows. In the flow regimes where the analyses are appropriate, the predicted quadratic dependence of stresses upon shear rate is in fairly good agreement with laboratory measurements.

The intermediate flow regime, in which both nearly instantaneous collisional and longer time particle interactions are present and contribute to the generation of stresses, is very important as it encompasses many practical applications and real flow situations. However, it is much more difficult to handle theoretically and the only analytical attempts to do so have involved the patching together of results from

the two flow regimes mentioned above. Simple examples of this may be found in Savage (1983), Norem, Irgens & Schieldrop (1987) and in the more detailed analysis of Johnson & Jackson (1987). Savage (1983), for example, suggested that, for the case of a shear flow in a gravitational field, one might represent the total stresses as the linear sum of a rate-independent, dry friction part plus a rate-dependent 'viscous' part obtained from the high-shear-rate granular flow kinetic theories.

For a free surface flow of the kind of interest here with the x- and y-directions parallel and perpendicular to the bed plane, the ratio of shear stress p_{xy} to normal stress p_{yy} might be expressed

$$\tan\delta = \frac{p_{xy}}{p_{yy}} = \frac{p_s(\nu)\tan\delta_s(\nu) + f_2(\nu)\rho_p\sigma^2(\mathrm{d}u/\mathrm{d}y)^2}{p_s(\nu) + f_1(\nu)\rho_p\sigma^2(\mathrm{d}u/\mathrm{d}y)^2}, \tag{2.1}$$

where δ is the friction angle of the sheared granular material, u is the velocity component parallel to the bed, $p_s(\nu)$ is the quasi-static contribution to the normal stress p_{yy}, σ and ρ_p are respectively the diameter and mass density of the particles, and ν is the solids fraction (volume of solids/total volume) of the granular material.

In the limit of very small deformation rates this reduces to

$$\tan\delta = \tan\delta_s(\nu), \tag{2.2}$$

where δ_s is termed the quasi-static friction angle. For high deformation rates (2.1) tends to

$$\tan\delta = \frac{f_2(\nu)}{f_1(\nu)} = \tan\delta_D(\nu), \tag{2.3}$$

where $\delta_D(\nu)$ is the dynamic friction angle which typically appears from experimental measurements to be fairly close to δ_s.

Both annular-shear-cell tests and open-channel chute flows can be used to provide empirical information to determine the functions $p_s(\nu)$, $f_1(\nu)$ and $f_2(\nu)$ necessary to explicitly define (2.1). An example of such a determination may be found in Norem *et al.* (1987).

Annular-shear-cell tests using quartz particles and other geological materials have been performed to investigate rate effects by Novosad (1964), Bridgwater (1972), Savage & Sayed (1984), Hungr & Morgenstern (1984*b*), Hanes & Inman (1985) and by Buggisch and Stadler (Stadler & Buggisch 1985; Stadler 1986; Buggisch & Stadler 1986). These tests were performed by two quite different procedures. Savage & Sayed and Hanes & Inman used a procedure in which stresses were determined as a function of shear-rate at a constant value of solids fraction. This is the approach that a rheologist might choose. The usual procedure for obtaining such data is as follows (see Savage & Sayed 1984). A normal load is applied to generate a desired normal stress on the granular material contained within an annular trough in the lower portion of the shear cell. Material is sheared by differential rotation of the upper and lower parts of the cell. Rotation rate is increased (causing an expansion of the layer of granular material contained within the annular trough) until the desired mean ν is obtained. Measurements are made of the torque, from which the shear stress can be determined. Tests are then continued in a step-like fashion increasing the loading weights and rotation rates to obtain data for shear stress and normal stress as functions of rotational velocity (or apparent shear rate) for a constant mean solids concentration ν. For a constant ν, the stresses are found to depend roughly upon the square of the shear rate. When the ratio of shear stress to normal stress for constant ν from tests performed in this manner is plotted versus apparent shear rate,

considerable scatter can be present in the data. Nevertheless, very little rate-dependence in the stress ratio is usually observed. To quote from the paper of Hanes & Inman (1985): 'The standard deviations of the stress ratios are approximately 10% of the mean, supporting the concept of a nearly constant stress ratio (over a range of shear rates and applied normal stresses) for a given material.'

An alternative type of test procedure (which might be regarded as a soil mechanics approach) has been used for example by Novosad (1964), Bridgwater (1972), Hungr & Morgenstern (1984*b*) and Buggisch and Stadler (Stadler & Buggisch 1985; Stadler 1986; Buggisch & Stadler 1986). Typically they determined shear stress as a function of rotation rate for a constant applied normal stress. In such tests the mean solids concentration is not maintained constant but the thickness of the layer of material in the trough is free to change throughout the test. As rotation rate is increased the bed expands and the mean concentration decreases. Tests in which rotation rate is monotonically increased or decreased are quite consistent with little scatter for a given test. There can be differences between subsequent runs depending upon the initial consolidation of the material. This kind of test in which the mean concentration changes is not only very relevant to the avalanche problem of the present paper but also gives a clear indication of the velocity-dependence of the friction angle.

The tests carried out by Hungr & Morgenstern (1984*b*) were performed with geological materials at high normal stresses with the aim of testing hypotheses about the mobility of large rock avalanches. Tests were performed with sand, mixtures of sand and fine rock flour, and sand submerged in water. Their results were plotted in terms of strength envelopes consisting of curves of shear stress versus normal stress at a constant rotation rate. The data were very well represented by straight lines through the origin, demonstrating a Mohr–Coulomb behaviour with a constant friction angle. There was little rate-dependence even though rotation rate was varied by three orders of magnitude. Hungr & Morgenstern were quite emphatic in their conclusions. 'These results indicate an absence of rate and normal stress effects over a range of conditions and material characteristics that do not leave much room for exceptions. Their significance is simple: the hypothesis of mechanical fluidization, postulating a breakdown of the Coulomb relationship at high velocities, although intuitively attractive, is not correct.'

Recently Buggisch and Stadler (Stadler & Buggisch 1985; Stadler 1986; Buggisch & Stadler 1986) have performed numerous careful tests with a sophisticated annular shear cell. Experiments have been performed with a variety of granular materials including glass beads, limestone powder and various plastic particles, the materials being in the dry state as well as at various levels of saturation (up to 100%) with liquids of different viscosities. Measurements of shear stress versus rotation rate for a constant normal stress show little rate dependence for the dry particles over a wide range of values of normal stress. Figure 1, which has been reproduced from Stadler (1986), shows some typical results for low normal stresses. The curves for the different normal stresses shown are very consistent with little scatter and show only a small increase of shear stress with velocity.

The annular-shear-cell results mentioned above should be examined to determine the flow regimes to which they correspond. Obviously, if the shear rates (non-dimensionalized in some appropriate fashion) are sufficiently small that the flow is in the quasi-static flow regime where particle inertia effects are negligible, then a lack of rate-dependence would not be surprising.

For the case of steady shearing flows a convenient non-dimensional parameter

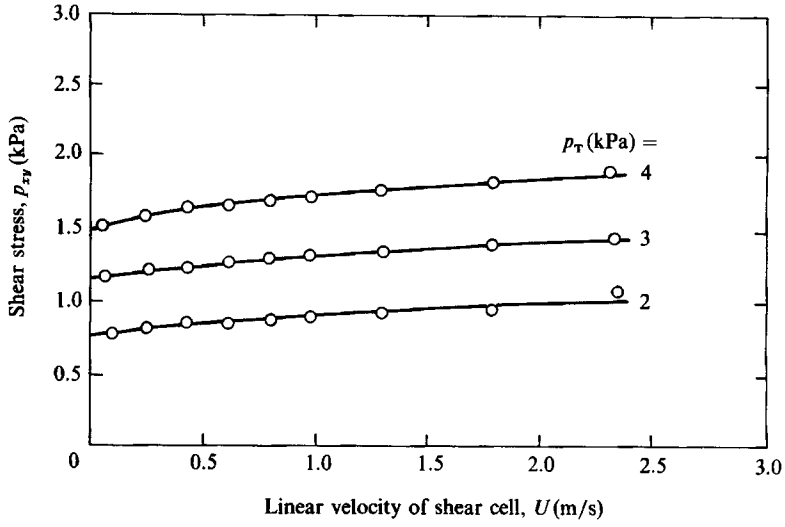

FIGURE 1. Shear stress p_{xy} versus linear velocity of shear cell U at constant applied normal stress p_T for 1.1 mm dry glass beads (Stadler 1986).

which characterizes the extent of fluidization and the importance of collisional stresses is the ratio

$$R_s = \frac{\rho_p \sigma^2 (U/H_s)^2}{p_T},$$

where U is the velocity difference across the shear layer and H_s is the shear-layer thickness. The numerator is proportional to the collisional normal stress and the denominator p_T is the total normal stress. Very small values of R_s correspond to a dominance of stresses generated by Coulomb dry frictional interactions and larger values (close to unity) of R_s correspond to vigorous particle velocity fluctuations, nearly instantaneous collisions and generation of stresses primarily by collisional interactions.

The tests of Savage & Sayed (1984) and Hanes & Inman (1985) at the lower concentrations and higher shear rates are generally regarded as being in the 'grain inertia' regime where collisional stresses are dominant. The measured shear stresses at constant solids concentrations show a nearly square dependence upon shear rate. The magnitudes of the stresses are reasonably close to those predicted by the granular-flow theories which postulate nearly instantaneous binary collisions.

Table 1 shows some estimates of the largest values of R_s for different values of solids fraction in the glass-bead experiments of Savage & Sayed (1984) and Hanes & Inman (1985). To calculate the values of R_s shown we have used the largest values of U and applied normal stress p_T at a given solids concentration ν. The values of R_s are somewhat larger in the tests of Savage & Sayed but are still roughly similar to those for the data of Hanes & Inman. As a very crude guide we can conclude from this table that values of R_s greater than about 0.1 correspond to the 'fluidized' state in which collisional interactions play a dominant role.

We now examine the shear-cell data of Hungr & Morgenstern and Buggisch & Stadler; both studies showed little or no dependence of shear stress upon shear rate. Consider first the sand-particle tests of Hungr & Morgenstern (1984*b*) which have the greatest chance of being in the fluidized state, i.e. have the largest value of R_s. For example, consider the case of sand particles of 1.5–2 mm diameter, the highest shear

Investigators	Savage and Sayed (1984)		Hanes & Inman (1985)			
Particle dia. (mm)	1.80		1.1		1.85	
solids fraction, ν	0.522	0.477	0.56	0.37, 0.42, 0.46	0.49	0.44
R_s	0.17	0.38	0.036	0.26	0.11	0.22

TABLE 1. Values of $R_s = \rho_p \sigma^2 (U/H_s)^2 / p_T$ in annular-shear-cell experiments of Savage & Sayed (1984) and Hanes & Inman (1985)

velocity of 0.98 m/s and the lowest normal stresses of about 20 kPa. While the cell depth was 20 mm, the height of the shear layer is not known. Roughly estimating it to be about 7 particle diameters yields a value of 0.0028 for R_s. The normal stress levels in these tests are so large that the grain inertia effects are comparatively quite small and the flow can be regarded as effectively in the quasi-static regime. Thus we can conclude little about rate effects on the basis of these data since the effective shear rates are too low.

Buggisch and Stadler were able to observe the thickness of the layer of sheared particles and found it to be between 4 and 7 particle diameters. Thus, for the normal stress of 2 kPa shown in figure 1 for 1.1 mm diameter glass beads, R_s would range roughly between 0.15 and 0.45. Comparing this with the values of R_s shown in table 1, we can conclude that the test data shown in figure 1 at the higher shear rates are in the fluidized grain inertia regime. The data thus cover the extremes of the flow regimes from the quasi-static flows, characterized by enduring interparticle contacts, to the fully fluidized, collision dominant grain inertia flows. Most importantly they show only a small rate-dependence in which shear stress increases only slightly with shear rate.

Chute flows can be used as another means to obtain information about constitutive behaviour that is relevant to the present granular avalanche problem. For steady two-dimensional fully developed free surface flow down a plane inclined at an angle ζ to the horizontal it can be shown that the ratio of the shear stress to the normal stress perpendicular the inclined plane must be equal to $\tan\zeta$ throughout the depth (Savage 1983). Since the bed normal stress corresponds to the weight of the layer of granular material, by increasing the bed inclination sufficiently, it is easy to generate well-fluidized flows in the grain inertia regime for small depths of material. Typically it is observed (see the annular-shear-cell tests mentioned earlier) that the ratio of shear to normal stress increases slightly with decrease in solids fraction ν. Hence, as bed inclination angle increases the velocities increase, dilation occurs and the increase in the dynamic friction angle makes it possible for a steady-state fully developed flow to exist at the larger value of ζ. If the inclination angle is increased to an angle greater than the dynamic friction angle that the material can develop, then the flow will continually accelerate down the chute. The range of dynamic friction angles that can be developed seems to depend upon the particular granular material. The range of chute inclination angles that permitted non-accelerating flow in the polystyrene bead tests of Savage (1979) and Hungr & Morgenstern (1984*a*) is about 10°. We note that the constitutive behaviour which can be inferred from these chute flows is quite consistent with that observed in the polystyrene-bead annular-shear-cell tests of Savage & Sayed (1984). Chute tests with some other materials have shown that steady flows were possible for a very much smaller range of inclination

angles. Augenstein & Hogg (1978), in their experiments with sand particles, found steady chute flows for only a single inclination angle. Bailard (1978), who also tested sand particles, obtained steady flows for a range of inclination angles from 34° to 39°.

It is also possible to determine the friction angle for accelerating chute flows for chute inclinations steeper than that required for steady non-accelerating flow (for example, see Knight 1983 and Hungr & Morgenstern 1984*a*). Knight found that the bed friction angle δ for spray-dried detergent was constant, independent of velocity, even for very highly accelerating flows where the material becomes very dilated as it flows down the chute. Hungr & Morgenstern (1984*a*) determined the ratio of bed shear stress to normal stress as a function of average chute flow velocity both indirectly by considering flow acceleration and directly by measuring wall stress over a section of the chute. Tests were performed with Ottawa sand, mixtures of sand and rock flour, and polystyrene beads. The polystyrene-bead data showed relatively little scatter and, as noted earlier, a gradual increase in shear to normal stress ratio with chute flow velocity. The data for the sand and sand–rock flour mixture from both the direct measurement and from the acceleration tests contained a scatter that exceeded the estimated error bounds. The authors could find no explanation for the unexpected magnitude of this scatter. Hungr & Morgenstern concluded that their chute flow data showed '... no systematic dependence on shear strain rate'.

As a final remark we note that in small-scale laboratory tests using small particles at high inclination angles in the splashing flow regime (Savage 1983; Ishida, Hatano & Shirai 1980) where vigorous saltation occurs and a low-density cloud of particles is present at the top surface, air drag effects become significant and act to restrain the particle velocities. This can give rise to a rate-dependence which is not likely to be present in geophysical-scale field events involving much larger particles.

2.1.2. *Assumption of rate-independence for bed friction angle*

The data discussed in the previous section show that the dependence of the bed friction angle δ on shear rate is generally quite weak. While the data for flow of polystyrene beads show a gradual but observable increase of δ with shear rate, the data for tests with glass beads, sand, and sand–rock flour mixtures (which are probably more typical of the behaviour of real geological materials) show only a very small, and in some cases not observable, dependence upon shear rate. The data cover the range of flows from the quasi-static to the grain inertia regimes.

In the present paper, which deals with dry cohesionless granular materials, we shall assume that the bed friction angle δ is constant, independent of shear rate and solids concentration. This assumption can result in major simplifications in the analysis of the granular avalanche motion. By performing depth averaging we need only be concerned, for example, with quantities such as stresses at the bed rather than the distribution of stress throughout the depth. When the pile is long and thin and slowly varying, the normal stress at the bed is determined by the depth of the overburden. Through the bed friction angle (which we assume to be rate-independent) we can determine the bed shear stress. By use of the depth averaging we avoid the need to consider the detailed character of the flow and avoid the complexities inherent in an analysis that uses a constitutive equation based upon, say, the kinetic theories of granular flows. A kinetic-theory approach would involve solution of an additional energy equation, solutions for granular temperatures, velocity and density variations. These solutions would involve the use of the very complex boundary conditions for granular temperatures, velocities, stresses, etc. It has been

demonstrated by Szidarovszky, Hutter & Yakowitz (1987) that the construction of solutions to the related problem of chute flows (Savage 1979) is very difficult.

2.1.3. *Velocity and density profiles*

Melosh (1986) has reviewed field data from very large landslides and concluded that the evidence suggested sliding on a thin basal layer. The basal zone is the active zone where the shear rates are high and nearly all the shear takes place. Thus the velocity profile is expected to be quite blunt and the depth-averaged streamwise velocity is quite close to the actual velocity everywhere except at the very base. Furthermore, since the vigorous shearing, fluidization and significant density variations are confined to a thin basal layer, it is sufficiently accurate to use a constant depth-averaged value for the density in our computations.

2.2. *Detailed derivation*

We now continue with the development of the governing equations. Consider free surface flow of a granular material along a slowly varying bottom profile (see figure 2). We assume that the granular material can be treated as a continuum which implies that the thickness h of the sliding and deforming body extends over several particle diameters. Moreover, for the reasons just explained, we shall ignore variations of the density due to changes of the void ratio within the avalanche. Under these conditions an incompressible model, consisting of the balances of mass and momentum, namely

$$\left.\begin{aligned} \boldsymbol{\nabla}\cdot\boldsymbol{u} &= 0, \\ \rho\frac{\mathrm{d}\boldsymbol{u}}{\mathrm{d}t} &= -\boldsymbol{\nabla}\cdot\boldsymbol{p}+\rho\boldsymbol{g}, \end{aligned}\right\} \tag{2.4}$$

may be used to describe the motion of the avalanching mass. In these equations $\boldsymbol{u}$ is the velocity vector, ρ the constant density, $\boldsymbol{p}$ the pressure tensor and $\boldsymbol{g}$ the vector of gravitational acceleration. Through a constitutive relation the pressure tensor $\boldsymbol{p}$ and the motion $\boldsymbol{u}$ can be functionally related.

Boundary conditions at the free surface may be expressed in terms of a function $F_{\mathrm{S}}(\boldsymbol{x},t)$ which is zero for a particle there, i.e.

$$\left.\begin{aligned} \frac{\partial F_{\mathrm{S}}}{\partial t}+\boldsymbol{\nabla}F_{\mathrm{S}}\cdot\boldsymbol{u} &= 0, \\ \boldsymbol{p}\cdot\boldsymbol{n} &= 0, \end{aligned}\right\} \quad \text{at} \quad F_{\mathrm{S}}(\boldsymbol{x},t)=0. \tag{2.5}$$

The first is the kinematic statement that the free surface is material, the second expresses stress-free conditions, and $\boldsymbol{n}$ is the exterior unit normal vector.

Similarly for a 'particle' at the base, such that $F_{\mathrm{B}}(\boldsymbol{x})=0$, the statement $\boldsymbol{u}\cdot\boldsymbol{n}=0$ expresses the tangency of the flow. Furthermore, we assume a solid friction law, which relates shear traction S to the local friction angle δ and the normal stress N, $S=\pm N\tan\delta$, where the sign is given by the direction of the sliding velocity. With

$$S=\boldsymbol{n}\cdot\boldsymbol{p}-\boldsymbol{n}(\boldsymbol{n}\cdot\boldsymbol{p}\cdot\boldsymbol{n}),$$

and

$$N=\boldsymbol{n}\cdot\boldsymbol{p}\cdot\boldsymbol{n}$$

the two boundary conditions become

$$\left.\begin{aligned} &\boldsymbol{u}\cdot\boldsymbol{n}=0 \\ &\boldsymbol{n}\cdot\boldsymbol{p}-\boldsymbol{n}(\boldsymbol{n}\cdot\boldsymbol{p}\cdot\boldsymbol{n})=-\left(\frac{\boldsymbol{u}_{\mathrm{s}}}{|\boldsymbol{u}_{\mathrm{s}}|}\right)(\boldsymbol{n}\cdot\boldsymbol{p}\cdot\boldsymbol{n})\tan\delta \end{aligned}\right\} \quad \text{at} \quad F_{\mathrm{B}}(\boldsymbol{x})=0. \tag{2.6}$$

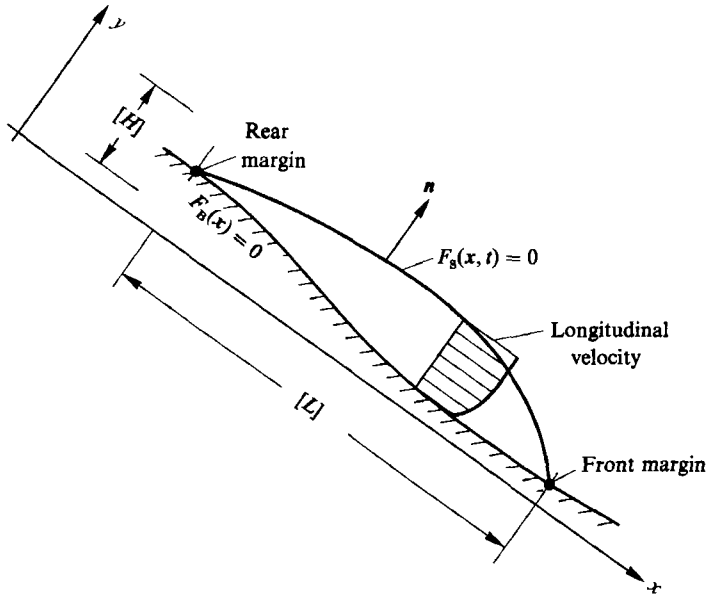

FIGURE 2. Sketch of the geometry of a finite mass of granular material moving along a curved rigid bed showing definitions of the free surface given by $F_S(x, t) = 0$ and the equation of the bed $F_B(x) = 0$. Also indicated are the scales $[L]$ and $[H]$ for the spread and maximum height.

where $\boldsymbol{u}_s$ is the sliding velocity relative to the stationary bed. Equations (2.4)–(2.6) comprise the complete boundary-value problem.

We now introduce the plane Cartesian coordinates x and y (see figure 2). In this coordinate system the field equations (2.4) become

$$\frac{\partial u}{\partial x}+\frac{\partial v}{\partial y}=0, \tag{2.7a}$$

$$\rho\left\{\frac{\partial u}{\partial t}+u\frac{\partial u}{\partial x}+v\frac{\partial u}{\partial y}\right\}=\rho g\sin\zeta-\frac{\partial p_{xx}}{\partial x}-\frac{\partial p_{xy}}{\partial y}, \tag{2.7b}$$

$$\rho\left\{\frac{\partial v}{\partial t}+u\frac{\partial v}{\partial x}+v\frac{\partial v}{\partial y}\right\}=-\rho g\cos\zeta-\frac{\partial p_{xy}}{\partial x}-\frac{\partial p_{yy}}{\partial y}. \tag{2.7c}$$

The mean inclination angle, denoted by ζ, is constant.

It is advantageous to non-dimensionalize the equations by scaling variables accordingly. To this end let

$$\left.\begin{aligned}(x, y) &= ([L]x^*, [H]y^*),\\ (u, v, t) &= \left([(gL)^{\frac{1}{2}}]u^*, \left[\frac{H}{L}(gL)^{\frac{1}{2}}\right]v^*, \left(\frac{L}{g}\right)^{\frac{1}{2}}t^*\right),\\ (p_{xx}, p_{yy}, p_{xy}) &= [\rho g\cos\zeta H]\,(p^*_{xx}, p^*_{yy}, \tan\zeta p^*_{xy}).\end{aligned}\right\} \tag{2.8}$$

Quantities in square brackets are typical values for the variable in question and variables having an asterisk are dimensionless and are taken to be of order unity. We have scaled quantities in the x- and y-directions differently; $[L]$ is a typical span or spread of the slide and $[H]$ a typical depth. Observations indicate that the aspect

ratio $\epsilon = [H/L]$ is small. This scaling is different from the well-known shallow-water scaling. The longitudinal velocity scale is $(gL)^{\frac{1}{2}}$, which indicates that the phenomenon is governed chiefly by free fall rather than by surface waves (which would require the use of $(gH)^{\frac{1}{2}}$). In ensuing developments we shall define the free surface and the bed by $y = h(x,t)$ and $y = b(x)$; h and b will be scaled respectively by $[H]$ so that

$$h(x,t) = [H]h^*(x^*, t^*), \quad b(x) = [H]b^*(x^*). \tag{2.9}$$

Both, h^* and b^* as well as $\partial h^*/\partial x^*$, $\mathrm{d}b^*/\mathrm{d}x^*$ will be assumed to be order-unity functions. This latter assumption on the derivatives is equivalent to the assumption of slow variation of the bed and the free surface since $\partial h/\partial x$ and $\mathrm{d}b/\mathrm{d}x$ are order ϵ. With (2.8) and (2.9), (2.7) take on the form

$$\frac{\partial u}{\partial x} + \frac{\partial v}{\partial y} = 0, \tag{2.10a}$$

$$\frac{\partial u}{\partial t} + u\frac{\partial u}{\partial x} + v\frac{\partial u}{\partial y} = \sin\zeta\left(1 - \frac{\partial p_{xy}}{\partial y}\right) - \epsilon\cos\zeta\frac{\partial p_{xx}}{\partial x}, \tag{2.10b}$$

$$\epsilon\left\{\frac{\partial v}{\partial t} + u\frac{\partial v}{\partial x} + v\frac{\partial v}{\partial y}\right\} = -\cos\zeta\left(1 + \frac{\partial p_{yy}}{\partial y}\right) - \epsilon\sin\zeta\frac{\partial p_{xy}}{\partial x}, \tag{2.10c}$$

in which for brevity asterisks have been omitted; subsequently this will always be done.

In the limit as $\epsilon \to 0$, (2.10c) reduces to the hydrostatic equilibrium equation, yielding

$$p_{yy}(x,y,t) = h(x,t) - y \tag{2.11}$$

after integration and taking account of the zero pressure condition at the free surface.

The shallowness or long-wave limit $\epsilon \to 0$ leads to an x-momentum equation in which one is tempted to ignore longitudinal stress gradients (i.e. the last term in (2.10b) would be dropped). The emerging set of equations is, however, too simple to model avalanche motions properly. Obviously, while the dimensionless pressure is an order-unity function, $\partial p_{xx}/\partial x$ is sufficiently large that $\epsilon\,\partial p_{xx}/\partial x$ is non-negligible. On the other hand, in the transverse momentum equation, $\epsilon\,\partial p_{xy}/\partial x$ and the transverse acceleration are small and negligible so that $\epsilon \to 0$ implies the hydrostatic pressure assumption. The procedure to be used in the present analysis is as follows. We shall depth average the x-momentum equation which, after further simplification, will eventually contain terms involving the bed shear stress and the integral over the depth of the normal stress p_{xx}. The latter term (corresponding to the last term of (2.10b) is of order ϵ. We shall relate p_{xx} and p_{yy} to one another throughout the depth and relate p_{xy} to p_{yy} at the bed through the use of constitutive assumptions. Thus it is consistent (to order ϵ) to obtain an order-unity expression for p_{yy} (as in (2.11)), determine p_{xx} from it through the constitutive assumption, and finally use this expression for p_{xx} in the last (order ϵ) term of the depth-averaged (2.10b). This will yield a final set of equations which is accurate to order ϵ. Such scaling arguments are well established in the glaciological literature where it is recognized that the longitudinal stress variations (the last term on the right-hand side of (2.10b) are non-negligible when sliding is significant in comparison to differential shear (Fowler 1980, 1984 unpublished). We could in a second step improve the overburden pressure by

substituting the results obtained for u, v and p_{xy} and evaluating a correction to p_{yy} according to

$$\text{corr}\,(p_{yy}) = \frac{\epsilon}{\cos\zeta}\int_y^h \left\{\frac{\partial v}{\partial t}+u\frac{\partial v}{\partial x}+v\frac{\partial v}{\partial y}+\sin\zeta\frac{\partial p_{xy}}{\partial x}\right\}\mathrm{d}y. \tag{2.12}$$

In this spirit we now proceed. In a first step (2.10b) is integrated from $y = b$ to $y = h$. Making use in this process of the continuity equation and using Leibnitz's rule when interchanging differentiations and integrations, it is found that

$$\frac{\partial}{\partial t}\int_b^h u\,\mathrm{d}y+\frac{\partial}{\partial x}\int_b^h u^2\,\mathrm{d}y-\left[u\left(\frac{\partial h}{\partial t}+u\frac{\partial h}{\partial x}-v\right)\right]_{\text{free surface}}+\left[u\left(u\frac{\mathrm{d}b}{\mathrm{d}x}-v\right)\right]_{\text{base}}$$

$$=\sin\zeta[(h-b)-p_{xy}(h)+p_{xy}(b)]-\epsilon\cos\zeta\left[\frac{\partial}{\partial x}\int_b^h p_{xx}\,\mathrm{d}y-p_{xx}(h)\frac{\partial h}{\partial x}+p_{xx}(b)\frac{\mathrm{d}b}{\mathrm{d}x}\right]. \tag{2.13}$$

Several terms in this expression vanish in view of the boundary conditions which are imposed at the free surface and the bed. The kinematic conditions read

$$\left.\begin{aligned}\frac{\partial h}{\partial t}+u\frac{\partial h}{\partial x}-v=0 \quad &\text{at} \quad y=h(x,t),\\ u\frac{\partial b}{\partial x}-v=0 \quad &\text{at} \quad y=b(x).\end{aligned}\right\} \tag{2.14}$$

Second, the stress condition (2.5) at the free surface $y = h(x, t)$ expressed in terms of dimensionless coordinates reads

$$-\epsilon\cos\zeta p_{xx}\frac{\partial h}{\partial x}+\sin\zeta p_{xy}=0, \quad -\epsilon\sin\zeta p_{xy}\frac{\partial h}{\partial x}+\cos\zeta p_{yy}=0 \quad \text{at} \quad y=h(x,t).$$

Consideration of the constitutive relationship given below (cf. (2.19) and (2.20) and figure 3) at the stress free surface yields $p_{xx} = k_{\text{actpass}}\,p_{yy}$ so the last two equations imply

$$p_{xy}=p_{yy}=0 \quad \Rightarrow \quad p_{xx}=0 \quad \text{at} \quad y=h(x,t). \tag{2.15}$$

With (2.14) and (2.15), (2.13) simplifies and becomes

$$\frac{\partial}{\partial t}\int_b^h u\,\mathrm{d}y+\frac{\partial}{\partial x}\int_b^h u^2\,\mathrm{d}y=\sin\zeta(h-b)+\sin\zeta p_{xy}|_{\text{base}}-\epsilon\cos\zeta\left[\frac{\partial}{\partial x}\int_b^h p_{xx}\,\mathrm{d}y+p_{xx}(b)\frac{\mathrm{d}b}{\mathrm{d}x}\right]. \tag{2.16}$$

We now define the transverse averages

$$\left.\begin{aligned}&\bar{u}\hat{h}=\int_b^h u\,\mathrm{d}y, \quad \bar{p}_{xx}\hat{h}=\int_b^h p_{xx}\,\mathrm{d}y, \quad \bar{p}_{yy}\hat{h}=\int_b^h p_{yy}\,\mathrm{d}y,\\ &\overline{u^2}\hat{h}=\int_b^h u^2\,\mathrm{d}y=\alpha_1\bar{u}^2\hat{h},\end{aligned}\right\} \tag{2.17}$$

in which $\hat{h} = h-b$ is the depth. Values of α_1 which deviate from unity give information about the deviation of the velocity profile from uniformity. To give some idea of numerical values for α_1 note that for a parabolic veloeity profile with vanishing basal velocity (corresponding to no sliding, all differential shear)

$$\alpha_1=\tfrac{6}{5}.$$

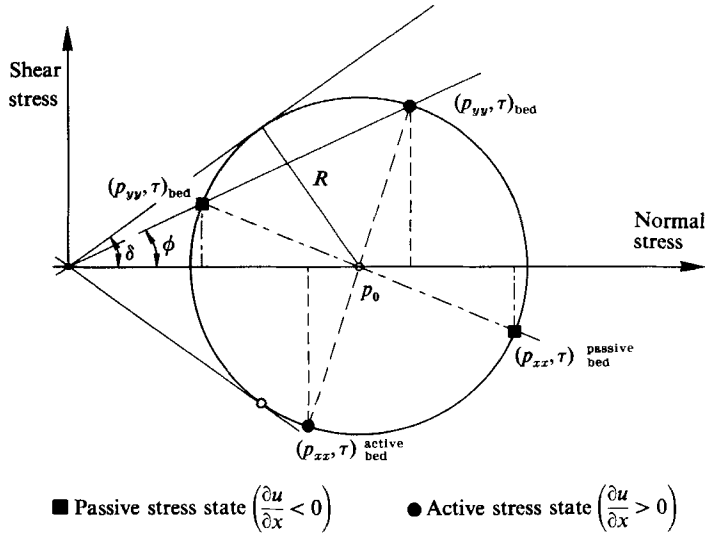

FIGURE 3. Mohr diagram showing Coulomb yield criterion, bed friction angle, and active and passive stress conditions.

whereas for a uniform profile (all sliding and no differential shear)

$$\alpha_1 = 1.$$

Since it is likely that sliding is present, the active shear zone is confined to a thin basal layer and the velocity profile is blunt (Melosh 1986), we may, without introducing a large error, choose $\alpha_1 \approx 1$.

With our shallowness assumption the non-dimensional form of the Coulomb sliding law (2.6) becomes

$$p_{xy} = -\operatorname{sgn}(\bar{u}) p_{yy} \cot\zeta \tan\delta + O(\epsilon^2) \quad \text{at} \quad y = b(x). \tag{2.18}$$

The final statement that is needed is a constitutive relationship for the pressure tensor. On the basis of the earlier discussion we assume the granular pile to behave as a cohesionless Mohr–Coulomb type material (see, for example, Roscoe 1970) described by a constant internal friction angle ϕ. Thus yielding will occur at a point on a plane element when

$$|S| = N \tan\phi, \tag{2.19}$$

where S and N are respectively the shear and normal stress acting on the element. The bed shear stress was previously expressed in analogous fashion in terms of a constant basal friction angle δ (see (2.6)). This assumed constitutive behaviour is shown graphically by means of a standard Mohr diagram in figure 3. We assume that an active or passive state of stress is developed depending upon whether an element of material is being elongated or compressed in the direction parallel to the bed. Thus the stresses normal and parallel to the mean inclination angle may be related in standard fashion through the use of an earth pressure coefficient, k_{actpass}, thus

$$p_{xx} = k_{\text{actpass}} p_{yy}, \tag{2.20}$$

where $k_{\text{actpass}} = k_{\text{act}}$ or k_{pass}, and from figure 3 it may easily be shown that

$$\left.\begin{matrix} k_{\text{act}} \\ k_{\text{pass}} \end{matrix}\right\} = 2[1 \mp (1-(1+\tan^2\delta)\cos^2\phi)^{\frac{1}{2}}]/\cos^2\phi - 1 \quad \text{for} \quad \partial\bar{u}/\partial x = \gtrless 0. \tag{2.21}$$

Incorporating (2.17)–(2.20) into (2.16) yields

$$\frac{\partial}{\partial t}(\hat{h}\bar{u})+\frac{\partial}{\partial x}(\alpha_1\hat{h}\bar{u}^2)=\sin\zeta\hat{h}-\epsilon\cos\zeta k_{\text{actpass}}\left[\frac{\partial}{\partial x}(\hat{h}\bar{p}_{yy})+p_{yy}(x,b)\frac{\mathrm{d}b}{\mathrm{d}x}\right]$$
$$-\cos\zeta\,\mathrm{sgn}(\bar{u})p_{yy}(x,b)\tan\delta. \quad (2.22)$$

The overburden pressure is obtained from (2.11)

$$\left.\begin{aligned} p_{yy}(x,b)&=h(x,t)-b(x)=\hat{h}(x,t),\\ \hat{h}\bar{p}_{yy}(x,t)&=\tfrac{1}{2}(h(x,t)-b(x))^2=\tfrac{1}{2}\hat{h}^2(x,t),\end{aligned}\right\} \quad (2.23)$$

so that (2.22) now becomes

$$\frac{\partial}{\partial t}(\hat{h}\bar{u})+\frac{\partial}{\partial x}(\alpha_1\hat{h}\bar{u}^2)=\sin\zeta\hat{h}-\cos\zeta\,\mathrm{sgn}\,(\bar{u})\tan\delta\,\hat{h}-\epsilon\cos\zeta\,k_{\text{actpass}}\left[\frac{\partial}{\partial x}\left(\frac{\hat{h}^2}{2}\right)+\hat{h}\frac{\mathrm{d}b}{\mathrm{d}x}\right]. \quad (2.24)$$

Finally, if we integrate the continuity equation (2.7*a*) over the depth and use the kinematic boundary conditions at the free surface and at the base, we obtain

$$\frac{\partial\hat{h}}{\partial t}+\frac{\partial}{\partial x}(\hat{h}\bar{u})=0. \quad (2.25)$$

Using (2.25), (2.24) can be simplified to

$$\frac{\partial\bar{u}}{\partial t}+\bar{u}\frac{\partial\bar{u}}{\partial x}=\sin\zeta-\epsilon\cos\zeta\,k_{\text{actpass}}\left[\frac{\partial\hat{h}}{\partial x}+\frac{\mathrm{d}b}{\mathrm{d}x}\right]-\mathrm{sgn}\,(\bar{u})\cos\zeta\tan\delta, \quad (2.26)$$

where we have set $\alpha_1=1$.

Equations (2.25) and (2.26) comprise a system of two partial differential equations for the profile $\hat{h}(x,t)$ and the transversely averaged velocity $\bar{u}(x,t)$. Provided the internal angle of friction ϕ, the basal friction angle δ, and the basal geometry (through the angle ζ and the function $b(x)$) are known, the evolution in time of both $\hat{h}$ and $\bar{u}$ can be determined if an initial profile and a velocity distribution

$$h(x,0)=h_0(x),\quad \bar{u}(x,0)=\bar{u}_0(x),$$

are prescribed. Interestingly, except for the term in brackets in (2.26), (2.25) and (2.26) contain only the difference $\hat{h}=h-b$. Were it not for this term the basal profile would simply be superimposed on the avalanche depth. For the motion of an avalanche along a planar bed we may set $b=0$ and replace $\hat{h}$ by h. The considerations of the present paper will be restricted to this case, and we quote below the resulting equations which will be called system (I):

$$\left.\begin{aligned} &\frac{\partial h}{\partial t}+\frac{\partial}{\partial x}(hu)=0, && (2.27a)\\ &\frac{\mathrm{d}u}{\mathrm{d}t}=\frac{\partial u}{\partial t}+u\frac{\partial u}{\partial x}=(\sin\zeta-\tan\delta\,\mathrm{sgn}\,(u)\cos\zeta)-\beta\frac{\partial h}{\partial x}. && (2.27b)\end{aligned}\right\}\ (\mathrm{I})$$

Here we have omitted the overbars for simplicity. Furthermore,

$$\beta=\epsilon k_{\text{actpass}}\cos\zeta \quad (2.28)$$

is a small constant.

Boundary conditions which must be imposed upon (I) are

$$\left.\begin{aligned} h(x,t) &= h_{\mathrm{F}}(t) \quad x = x_{\mathrm{F}}(t), \\ h(x,t) &= h_{\mathrm{R}}(t) \quad x = x_{\mathrm{R}}(t). \end{aligned}\right\} \tag{2.29}$$

where $x_{\mathrm{F}}(t)$ and $x_{\mathrm{R}}(t)$ denote the front and rear margins respectively, and the depths $h_{\mathrm{F}}(t)$ and $h_{\mathrm{R}}(t)$ are prescribed functions of time. Note that $h_{\mathrm{F}}(t) = h_{\mathrm{R}}(t) = 0$ are obvious choices, but cliffs are also possible.

Finally, we mention that the margin velocities are given by

$$u_{\mathrm{F}} = \frac{\mathrm{d}x_{\mathrm{F}}}{\mathrm{d}t}, \quad u_{\mathrm{R}} = \frac{\mathrm{d}x_{\mathrm{R}}}{\mathrm{d}t}. \tag{2.30}$$

3. Similarity solutions

The basic idea in finding particular solutions to the moving-boundary-value problem of the last section is to apply a fixed domain mapping by which the span interval is mapped onto a fixed interval†, $[-1, 1]$. To this end, we define

$$u_0(t) = \int_0^t (\sin\zeta - \tan\delta\cos\zeta)\,\mathrm{d}t. \tag{3.1}$$

This corresponds to the velocity of a point mass and is the solution to system (I) for a rigid granular mass. We have assumed that the bed slope and bed friction angle are such that the $\operatorname{sgn}(\bar{u})$-term in (2.26) is always positive. We shall subsequently examine the restrictions on the solutions that this implies. The translation (see figure 4)

$$\xi = x - \int_0^t u_0(t')\,\mathrm{d}t' \tag{3.2}$$

shifts the origin of the frame (ξ, t), moving with velocity $u_0(t)$, to the location where $\partial h/\partial x = 0$. With (3.2) it is now also convenient to introduce the difference velocity

$$\tilde{u} = u - u_0(t) \tag{3.3}$$

as a new unknown. For the purposes of this similarity analysis we further suppose symmetry with respect to $\xi = 0$ of the depth profile and skew-symmetry of the difference velocity, viz.

$$h(\xi,t) = h(-\xi,t), \quad \tilde{u}(\xi,t) = -\tilde{u}(-\xi,t), \tag{3.4}$$

so that the front and rear margin positions are given by

$$\xi_{\mathrm{F}} = g(t), \qquad \xi_{\mathrm{R}} = -g(t). \tag{3.5}$$

It follows that under these restrictive conditions the fixed-domain mapping is given by

$$\eta = \frac{\xi}{g(t)} = \frac{1}{g(t)}\left\{x - \int_0^t u_0(t')\,\mathrm{d}t'\right\}, \quad \tau = t. \tag{3.6}$$

† Note that for the similarity solutions it is most convenient to choose the lengthscale $[L]$ to correspond to one-half of the length of the pile at some reference time, whereas for the numerical simulations presented later the lengthscale $[L]$ is taken to be the total initial length of the pile at time $t = 0$.

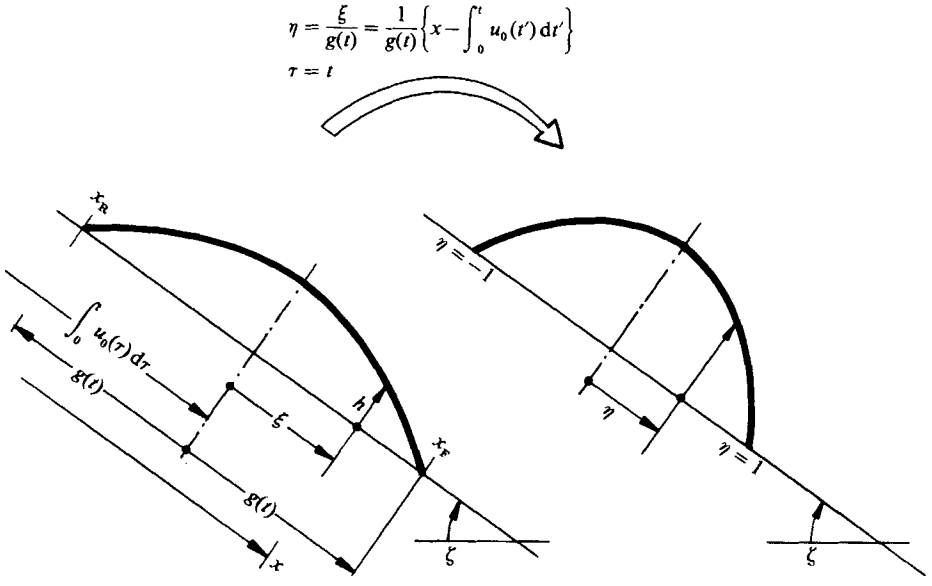

FIGURE 4. Explanation of the mapping of the space occupied by the granular mass in the physical domain to the fixed domain.

With the aid of these formulae we easily deduce

$$\frac{\partial}{\partial t} = \frac{\partial}{\partial \tau} - \left(\eta \frac{g'}{g} + \frac{u_0}{g}\right)\frac{\partial}{\partial \eta}, \quad \frac{\partial}{\partial x} = \frac{1}{g}\frac{\partial}{\partial \eta}. \tag{3.7}$$

Thus, system (I) assumes the alternative form

$$\left.\begin{aligned} \frac{\partial h}{\partial t} - \eta \frac{g'}{g}\frac{\partial h}{\partial \eta} + \frac{1}{g}\frac{\partial}{\partial \eta}(h\tilde{u}) = 0, & \qquad (3.8a) \\ \frac{\partial \tilde{u}}{\partial t} - \eta \frac{g'}{g}\frac{\partial \tilde{u}}{\partial \eta} + \frac{1}{g}\left(\tilde{u}\frac{\partial \tilde{u}}{\partial \eta} + \beta \frac{\partial h}{\partial \eta}\right) = 0. & \qquad (3.8b) \end{aligned}\right\} \text{(II)}$$

Here again we have replaced τ by t; moreover, the prime denotes univariate differentiation. The similarity solutions we present below are based on system (II).

3.1. *The parabolic cap*

Suppose we let

$$\tilde{u}(\eta, t) = \eta g'(t). \tag{3.9}$$

which is consistent with the symmetry requirement (3.4). With (3.9), (3.8*b*) reduces to

$$\frac{\partial h}{\partial \eta} = -\frac{gg''}{\beta}\eta,$$

or upon integration,

$$h = \frac{gg''}{2\beta}(1 - \eta^2), \tag{3.10}$$

in which the boundary conditions

$$h(\eta = \pm 1) = 0 \tag{3.11}$$

were invoked. For the present case the material elements are always expanding in the direction parallel to the bed, so the stress state corresponds to the active case and $k_{\text{actpass}} = k_{\text{act}}$.

Conservation of the total mass, M, in the pile requires that

$$\int_{\xi_R}^{\xi_F} h(\xi, t)\,\mathrm{d}\xi = \int_{-1}^{1} h(\eta, t)\, g(t)\,\mathrm{d}\eta = M.$$

Substituting (3.10) thus yields

$$g''g^2 = \tfrac{3}{2}\beta M = K. \tag{3.12}$$

This solution is consistent with (3.8a), as it can easily be demonstrated that with (3.10) and (3.12) the equation is identically satisfied. Alternatively, we could have substituted (3.10) into (3.8a) and obtained a differential equation for g for which a first integral would have led to (3.12). However, the physical interpretation of the constant of integration, K, would still have required a total mass balance statement.

We shall integrate (3.12) subject to the initial conditions

$$g(0) = 1.0, \quad g'(0) = 0 \tag{3.13}$$

corresponding to a pile of physical length $2L$ at rest at $t = 0$. Changing the independent variable in (3.12) from t to g and letting $p = g'$, (3.12) is seen to be equivalent to

$$p\,\mathrm{d}p = K\frac{\mathrm{d}g}{g^2} = -K\,\mathrm{d}\left(\frac{1}{g}\right),$$

from which, on imposing (3.13), a final integral is seen to be

$$p^2 = 2K(1 - 1/g). \tag{3.14}$$

Thus, since $p = \mathrm{d}g/\mathrm{d}t$, we obtain the separable equation

$$\frac{g^{\frac{1}{2}}\mathrm{d}g}{(g-1)^{\frac{1}{2}}} = (2K)^{\frac{1}{2}}\,\mathrm{d}t. \tag{3.15}$$

The substitution $g = z^2$, $\mathrm{d}g = 2z\,\mathrm{d}z$ will transform the term on the left-hand side to a standard, integrable form (see e.g., Dwight 1968, integral No. 262.01). The final solution of (3.15) subject to the initial condition $g(0) = 1$ reads

$$(g(g-1))^{\frac{1}{2}} + \ln|g^{\frac{1}{2}} + (g-1)^{\frac{1}{2}}| = (2K)^{\frac{1}{2}}t, \tag{3.16}$$

and defines t as a function of g. The inverse relationship is plotted in figure 5 for $M = \frac{4}{3}$ (corresponding to an initial profile $h(\xi, 0) = (1 - \xi^2)$) and the indicated values of the shallowness parameter β. Evidently, the lateral spread g is monotonically increasing with time and approaches a linear relationship as $g \to \infty$, namely $g \sim (2K)^{\frac{1}{2}}t$. Incidentally, the graphs in figure 5 were obtained by integrating (3.12) with the Runge–Kutta method, and the results were checked with the aid of (3.16).

The complete solution is now given by (3.9), (3.10) and (3.16). With the aid of (3.12) and (3.15) it can be written in the following parametric form:

$$\tilde{u}(\eta, t) = \left[\frac{2K}{g}(g-1)\right]^{\frac{1}{2}}\eta, \qquad h(\eta, t) = \frac{K}{g}(1 - \eta^2), \tag{3.17a, b}$$

where $g(t)$ can be deduced from (3.16). It is not difficult to extract from these the large-time behaviour.

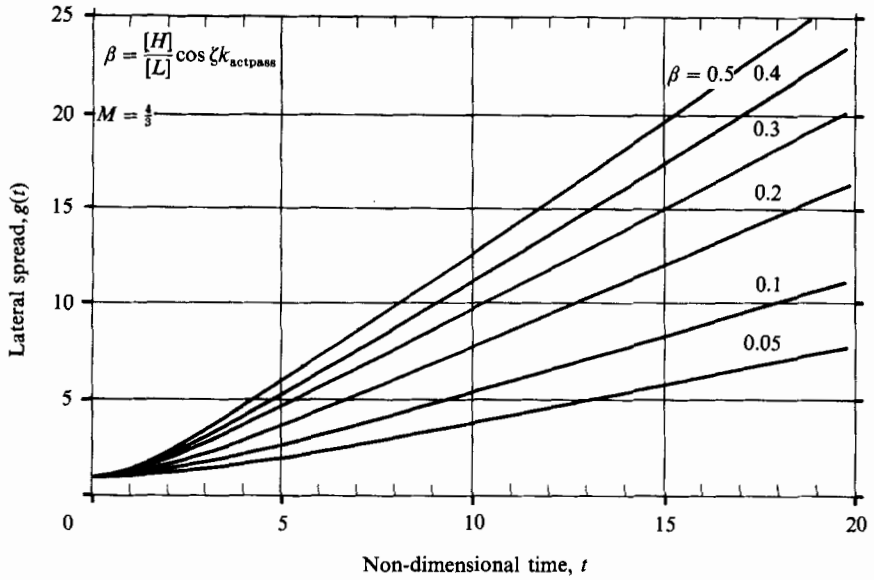

FIGURE 5. Lateral spread of the parabolic-cap solution as a function of dimensionless time. Note that g approaches a linear relationship when t becomes large.

Recall that it was assumed in the specification of the bed friction in the present similarity analysis that

$$u > 0. \tag{3.18}$$

This implies that $|\tilde{u}| < u_0$ or in other words

$$g' < u_0. \tag{3.19}$$

It is important to verify that the similarity solutions are consistent with this assumption. It is found that in some cases, for example for large values of ϵ, over a portion of the pile near the trailing edge at small time, condition (3.18) can be violated. Typically, as the flow develops the pile soon reaches a downstream position where condition (3.18) is then satisfied. Let us now determine this small-time consistency condition. Using $M = \frac{4}{3}$, (3.12) becomes

$$g''g^2 = 2\beta, \tag{3.20}$$

from which we find for small time

$$g' = 2\beta t. \tag{3.21}$$

For constant δ and ζ, (3.1) yields

$$u_0(t) = (\sin\zeta - \tan\delta\cos\zeta)t. \tag{3.22}$$

Substituting (3.21) and (3.22) into (3.19) gives the consistency condition at small time

$$\left.\frac{g'}{u_0}\right|_{t\to 0} = \frac{2\epsilon k_{\text{actpass}}\cos\zeta}{\sin\zeta - \tan\delta\cos\zeta} < 1, \tag{3.23}$$

This may be expressed in terms of an upper limit on ϵ for which the similarity solutions are consistent at small times. For example, for the case of $\delta = 15°, \phi = 30°$ and $\zeta = 30°$, (3.23) yields $\epsilon < 0.445$. Increasing ζ to 45° yields $\epsilon < 0.754$. Both of these

values for ϵ are probably greater than that for which the assumptions used in the derivation of the equations of motion are valid. Cases when ζ is close to δ yield smaller values for ϵ; values of $\delta = 22°$, $\phi = 29°$ and $\zeta = 32°$ corresponding to the experiment of Huber mentioned in §5.1 gives $\epsilon < 0.148$.

It can easily be shown that an entire family of similarity solutions related to (3.17) exists, not necessarily having zero margin depth but finite and constant normalized depth d_M. For these profiles (3.16) and (3.17*a*) still hold, but (3.17*b*) must be

$$h(\eta, t) = \frac{K}{g}(1 + d_M - \eta^2),$$

with

$$K = \frac{\frac{3}{2}\beta M}{1 + \frac{3}{2}d_M}. \tag{3.24}$$

3.2. *The* M-*wave*

Consider once more equations (II) and let us seek separation-of-variables solutions of the form

$$h(\eta, t) = l(t)H(\eta), \quad \tilde{u}(\eta, t) = k(t)F(\eta). \tag{3.25}$$

Substituting (3.25) into (3.8) yields

$$\left.\begin{aligned} H - \frac{g'l}{gl'}\eta H' + \frac{kl}{gl'}(HF)' &= 0, \\ F - \frac{g'k}{gk'}F' + \frac{k^2}{gk'}FF' + \frac{\beta l}{gk'}H' &= 0, \end{aligned}\right\} \tag{3.26}$$

which constitute two ordinary differential equations for H and F provided that

$$\frac{g'l}{gl'}, \quad \frac{kl}{gl'}, \quad \frac{g'k}{gk'}, \quad \frac{k^2}{gk'}, \quad \frac{l}{gk'} \tag{3.27}$$

are all constants. If we try the power solutions

$$g = t^\alpha, \quad l = t^\gamma, \quad k = t^\delta \tag{3.28}$$

it can easily be demonstrated that the five expressions in (3.27) are all time-independent if

$$\gamma = 2\delta \quad \text{and} \quad \delta = \alpha - 1. \tag{3.29}$$

A third relationship among the exponents α, γ and δ follows from the conservation of total volume:

$$\int_{-1}^{1} h(\eta,t)g(t)\,\mathrm{d}\eta = t^{\alpha+\gamma}\int_{-1}^{1} H(\eta)\,\mathrm{d}\eta \neq fn(t),$$

implying

$$\alpha + \gamma = 0. \tag{3.30}$$

From (3.28) and (3.29) we obtain

$$\alpha = \tfrac{2}{3}, \qquad \gamma = -\tfrac{2}{3}, \qquad \delta = -\tfrac{1}{3}, \tag{3.31}$$

$$g = t^{\frac{2}{3}}, \qquad l = t^{-\frac{2}{3}}, \qquad k = t^{-\frac{1}{3}}, \tag{3.32}$$

$$\eta = t^{-\frac{2}{3}}\xi, \quad h = t^{-\frac{2}{3}}H(\eta), \quad \tilde{u} = t^{-\frac{1}{3}}F(\eta). \tag{3.33}$$

Substituting (3.28) with (3.25) into (3.26) yields the ordinary differential equations

$$F'H + (F - \tfrac{2}{3}\eta)H' = \tfrac{2}{3}H, \quad (F - \tfrac{2}{3}\eta)F' + \beta H' = \tfrac{1}{3}F, \tag{3.34}$$

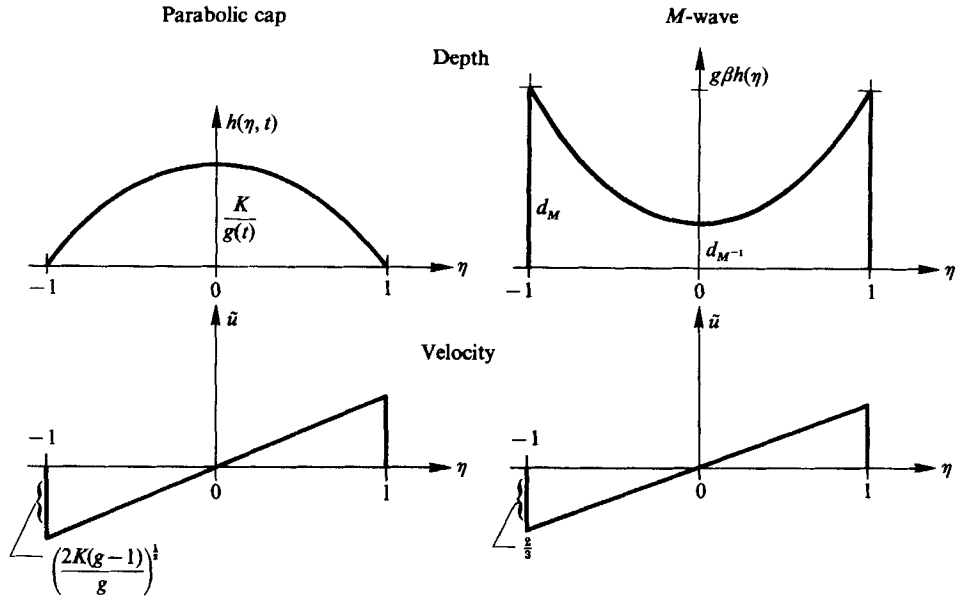

FIGURE 6. Shapes and velocity distributions of the parabolic-cap and the M-wave profiles in the fixed-domain space.

a simple solution of which is given by

$$F = \tfrac{2}{3}\eta, \quad H = \frac{1}{g\beta}(d_M - (1-\eta^2)), \quad d_M > 1. \tag{3.35}$$

Thus, the difference velocity $\tilde{u}$ is linearly distributed in η while the depth profile is parabolic as shown in figure 6. It is this shape which prompted us to label this solution as the 'M-wave'. The total volume M and d_M are related by

$$M = \frac{2}{g\beta}(d_M - \tfrac{2}{3}).$$

In summary, we have found two types of similarity solutions. The M-wave behaves as

$$\tilde{u} = \tfrac{2}{3}t^{-\frac{1}{3}}\eta, \quad h = \frac{1}{g\beta}t^{-\frac{2}{3}}(d_M - (1-\eta^2)); \tag{3.36}$$

$\tilde{u}$ and h decay with time, but the spread grows as $g = t^{\frac{2}{3}}$. The other, parabolic cap, solution (see figure 6) has a more complicated evolutionary behaviour and its asymptotic behaviour for large time is

$$\tilde{u} \sim (2K)^{\frac{1}{2}}\eta, \quad h \sim \left(\frac{K}{2}\right)^{\frac{1}{2}} t^{-1}(d_M + (1-\eta^2)), \tag{3.37}$$

with $g \sim (2K)^{\frac{1}{2}}t$. In this solution the difference velocity becomes time-independent as $t \to \infty$, and h decays as t^{-1}, while the spread grows linearly with t. The mean absolute asymptotic velocity of both waves is the same however, as both have the same $u_0(t)$.

Because we have assumed in this similarity analysis that u is always positive, the analysis is inconsistent at small times. Note that, in this instance, the inconsistency occurs for all values of ϵ not just for values greater than some limiting one, as in the

case of the parabolic-cap solution. Thus using (3.2) and (3.22) in (3.19) implies that the M-wave similarity solutions are only consistent for times

$$t > \left[\frac{2}{3(\sin\zeta - \tan\delta\cos\zeta)}\right]^{\frac{3}{4}}. \tag{3.38}$$

We note that this kind of breakdown of the similarity solutions for small times is not uncommon. For example, there exist similarity solutions for fluid-mechanical jets, plumes, etc. In any real physical situation these break down at the origin because they imply infinite velocities, point sources, etc. The relevance of the similarity solutions in these cases is that they can be regarded as asymptotes and in this context they are both useful and of interest. Note that, for example, the computations based upon the Lagrangian numerical approach described in §5.3 found that even significant perturbations to the similarity profile relax into the similarity solutions after a relatively short time. The analytical or semianalytical similarity solutions can also serve as means to check the validity of numerical integration schemes which we have found to be other than trivial to implement.

We remark in conclusion that the physical validity of the M-wave solutions must be viewed with some caution since the assumptions used for the derivation of the governing equations break down at the front and rear margins. On the other hand this situation is quite analogous to approaches commonly used in hydraulics. For example, in the study of roll waves which have steep fronts (Stoker 1957, pp. 461–469) the depth-averaged shallow-water wave equations are used over essentially the whole wavelength, and hydraulic jump conditions are used to join separate waves.

4. Considerations of stability

It is of interest to know how the avalanche depth profile would evolve from an initial profile of a roughly rectangular or triangular shape, in particular whether it would tend to approach either the parabolic-cap or M-wave similarity solutions. One's intuitive sense about the possible temporal development of the avalanche shape is likely to be confused. On one hand, no clear tendency to evolve into the M-wave profile is present in Huber's (1980) data and furthermore the more recent tests by Hutter *et al.* (1988) and K. Hutter, Ch. Plüss & S. B. Savage (paper in preparation) show a prevailing tendency to evolve towards the parabolic-cap similarity solution. On the other hand, these experimental data are not exhaustive and one is reluctant to rule out the possibility of M-wave solutions. The equations of motion used here are similar in form to the shallow-water wave equations in which nonlinearity causes wave steepening of the kind that would give rise to M-wave development. It was felt that stability analyses of both the parabolic-cap and the M-wave similarity solutions would not only give some qualitative information about the possible profile evolution but also might warn of possible numerical difficulties.

4.1. *Restricted small-perturbation analysis of the parabolic-cap solution*

In this section we prove that the parabolic-cap solution is stable against any small perturbation which leaves the spread g unperturbed. To this end let

$$\left.\begin{aligned} \tilde{u} &= u_0 + \hat{u} = \eta g'(t) + \hat{u}, \\ h &= h_0 + \hat{h} = \frac{1}{2\beta} g(t) g''(t)\,(1-\eta^2) + \hat{h}. \end{aligned}\right\} \tag{4.1}$$

(We only analyse the case $d_M = 0$.) As mentioned above, $g(t)$ is not perturbed and is given by (3.16). Substituting (4.1) into (3.8), rearranging and linearizing in the perturbation quantities (carrying the hat) yields

$$\left.\begin{aligned} \frac{\partial \hat{h}}{\partial t}+\frac{g''}{2\beta}(1-\eta^2)\frac{\partial \hat{u}}{\partial \eta}+\frac{g'}{g}\hat{h}-\frac{g''}{\beta}\eta\hat{u}=0,\\ \frac{\partial \hat{h}}{\partial t}+\frac{g'}{g}\hat{u}+\frac{\beta}{g}\frac{\partial \hat{h}}{\partial \eta}=0, \end{aligned}\right\} \tag{4.2}$$

from which the following single partial differential equation for $\hat{u}$ can be deduced:

$$\mathrm{L}_1(t)[\hat{u}]+\mathrm{D}_1(\eta)[\hat{u}]=0, \quad -1<\eta<1, \tag{4.3}$$

in which the operators $\mathrm{L}_1(t)[\cdot]$ and $\mathrm{D}_1(\eta)[\cdot]$ are given by

$$\left.\begin{aligned} \mathrm{L}_1(t)[\cdot]&=\frac{\partial}{\partial t}\left\{\frac{g^3}{K}\frac{\partial[\cdot]}{\partial t}\right\}+\left(2+\frac{gg'^2}{K}\right)[\cdot],\\ \mathrm{D}_1(\eta)[\cdot]&=2\eta\frac{\partial[\cdot]}{\partial \eta}-\frac{1}{2}(1-\eta^2)\frac{\partial^2[\cdot]}{\partial \eta^2}. \end{aligned}\right\} \tag{4.4}$$

Boundary conditions that must be imposed on (4.3) are

$$\hat{u}=0 \quad \text{at} \quad \eta=\pm 1, \tag{4.5}$$

while the initial conditions require the prescription of the η-distribution of $\hat{u}(\eta,0)$ and $\partial\hat{u}/\partial t(\eta,0)$. The exact form of these will not be needed in the sequel. Incidentally, (4.5) follows from the facts that $\tilde{u}(\pm 1,t)=g'(t)$ and $\hat{g}(t)=0$.

In view of the form of the operators L_1 and D_1 we look for a separation-of-variables solution

$$\hat{u}(\eta,t)=T(t)X(\eta). \tag{4.6}$$

With (4.6) the boundary-value problem (4.3)–(4.5) leads to the eigenvalue problem for X

$$\left.\begin{aligned} \mathrm{D}_1(\eta)[X(\eta)]+\lambda^2X(\eta)=0, \quad -1<\eta<1,\\ X(\eta)=0, \quad \eta=\pm 1 \end{aligned}\right\} \tag{4.7}$$

and the evolution equation for T

$$\left.\begin{aligned} \mathrm{L}_1(t)[T(t)]+\lambda^2T(t)=0,\\ T(0)=T_0, \quad T'(0)=T'_0. \end{aligned}\right\} \tag{4.8}$$

In these equations λ^2 is the separation constant, the eigenvalue to be determined. The expression for $X(\eta)$ provides the spatial distribution of $\hat{u}$ and $T(t)$ gives its evolution in time.

We solve the eigenvalue problem (4.7) first. To this end, let

$$x=\tfrac{1}{2}(1-\eta). \tag{4.9}$$

With this transformation $\eta\in[-1,1]$ is mapped on to $x\in[0,1]$ and the eigenvalue problem (4.7) becomes

$$\left.\begin{aligned} x(x-1)X''+(2-4x)X'+2\lambda^2X=0, \quad 0<x<1,\\ X(x)=0, \quad x=0,1. \end{aligned}\right\} \tag{4.10}$$

This is an eigenvalue problem of the hypergeometric differential equation. According to Abramowitz & Stegun (1964, pp. 562ff.), two independent solutions are

$$X_1 = F(a,b,c;x), \qquad X_2 = \ln x F(a,b,c;x) + P, \tag{4.11}$$

where

$$\left.\begin{array}{lll} c=2, & & c=2, \\ a+b+1=-4, & \Rightarrow & a=-\frac{5}{2}\left\{1\pm\left(1+\frac{8}{25}\lambda^2\right)^{\frac{1}{2}}\right\}, \\ ab=-2\lambda^2, & & b=-(a+5). \end{array}\right\} \tag{4.12}$$

In the above,

$$F(a,b,c;x) = \frac{\Gamma(c)}{\Gamma(a)\,\Gamma(b)} \sum_{n=0}^{\infty} \frac{\Gamma(a+n)\,\Gamma(b+n)}{\Gamma(c+n)} \frac{x^n}{n!} \tag{4.13}$$

is the hypergeometric function, Γ is the gamma function and P is a power series in x which is regular for $x \in [0,1]$. The power series (4.13) is convergent at $x=1$ provided that $c-a-b>0$ (which in fact equals 7), and X_2 defined in (4.11) is a solution of (4.10) as long as $|x| \leqslant 1$ and $a, b \neq 0$. Since $ab = -2\lambda^2$ and $\lambda \neq 0$ (as we shall see) the general solution of (4.10) is

$$X(x) = AX_1(x) + BX_2(x).$$

Regularity at $x=0$ requires $B=0$ and the boundary condition at $x=1$ demands $X_1(1)=0$, or (see Abramowitz & Stegun 1964, p. 556)

$$F(a,b,c;1) \equiv \frac{\Gamma(c)\,\Gamma(c-a-b)}{\Gamma(c-a)\,\Gamma(c-b)} = 0,$$

whence

$$\frac{\Gamma(2)\,\Gamma(7)}{\Gamma(2-a)\,\Gamma(7+a)} = 0. \tag{4.14}$$

Poles of $\Gamma(\cdot)$ are at $0, -1, -2, -3, \ldots$; so the eigenvalues are given by

$$a = 2,3,4,\ldots \quad \text{and} \quad a = -7,-8,-9,-10,\ldots.$$

With these and (4.12) we deduce

$$\lambda^2 = \tfrac{1}{2}a(a+5) \quad \Rightarrow \quad \lambda_n^2 = \tfrac{1}{2}(n+1)(n+6) > 0, \tag{4.15}$$

which are indeed positive numbers for all possible values of a (or $n = 1,2,\ldots$).

Next we use (4.8) to extract the stability statement. With (4.4), (4.8) can be written as

$$\frac{\mathrm{d}}{\mathrm{d}t}\left\{g^3(t)\frac{\mathrm{d}T}{\mathrm{d}t}\right\} + K\left(2+\frac{g(t)\,g'^2(t)}{K}+\lambda_n^2\right)T = 0. \tag{4.16}$$

To see whether the solution to this equation is asymptotically growing or decaying in time it suffices to analyse (4.16) for large time. Since $g(t) \sim (2K)^{\frac{1}{3}}t$ as $t \to \infty$, (4.16) reduces in this limit to the Euler equation

$$t^2T'' + 3tT' + T = 0 \quad (t \to \infty) \tag{4.17}$$

with the two independent solutions

$$T_{(1)} \sim t^{-1}, \quad T_{(2)} \sim t^{-1}\ln t \quad (t \to \infty), \tag{4.18}$$

both of which are vanishingly small for $t \to \infty$. This proves stability of the small perturbation of the parabolic-cap solution when $g(t)$ is left unperturbed.

4.2. *Restricted small-perturbation analysis of the* M*-wave solution*

In this subsection we demonstrate that the M-wave solution is stable against any small perturbation which leaves the spread g unperturbed.

Substituting the representations (4.1) (in which $g = t^{\frac{2}{3}}$) into (3.8), linearizing the emerging equations in the perturbation quantities and eliminating the variable $\hat{h}$ as before yields

$$\mathrm{L}_2(t)\,[\hat{u}] - \mathrm{D}_2(\eta)\,[\hat{u}] = 0 \tag{4.19}$$

as a partial differential equation for $\hat{u}$. The operators $\mathrm{L}_2(t)$ and $\mathrm{D}_2(\eta)$ are given by

$$\left.\begin{aligned} \mathrm{L}_2(t)\,[\cdot] &= t^2 \frac{\partial^2}{\partial t^2}[\cdot] + 2t\frac{\partial}{\partial t}[\cdot], \\ \mathrm{D}_2(\eta)\,[\cdot] &= \frac{4}{9}\eta\frac{\partial}{\partial \eta}[\cdot] + \beta\left(A + \frac{\eta^2}{9\beta}\right)\frac{\partial^2}{\partial \eta^2}[\cdot]. \end{aligned}\right\} \tag{4.20}$$

They are second order in time and space, respectively. As before the boundary conditions are $\hat{u} = 0$ for $\eta = \pm 1$. With

$$\hat{u}(\eta, t) = T(t)\,H(\eta) \tag{4.21}$$

(4.19) and (4.20) imply the eigenvalue problem for H

$$\left.\begin{aligned} \mathrm{D}_2(\eta)\,[(H(\eta)] + \lambda^2 H(\eta) = 0, \quad -1 < \eta < 1, \\ H(\eta) = 0, \quad \eta = \pm 1, \end{aligned}\right\} \tag{4.22}$$

and the initial-value problem for T

$$\left.\begin{aligned} \mathrm{L}_2(t)\,[T(t)] + \lambda_2 T(t) = 0, \quad t > 0, \\ T(0) = T_0, \quad T'(0) = T_0', \quad t = 0. \end{aligned}\right\} \tag{4.23}$$

Using a Rayleigh quotient argument all eigenvalues λ^2 of (4.22) can be shown to be positive. Using this same Rayleigh quotient an estimate for the smallest eigenvalue can be found to be $\lambda^2 > \frac{1}{4}$. The differential equation (4.23), or

$$t^2\frac{\mathrm{d}^2 T}{\mathrm{d}t^2} + 2t\frac{\mathrm{d}T}{\mathrm{d}t} + \lambda^2 T = 0 \tag{4.24}$$

is of equipotential (Euler) form and thus admits the two power solutions

$$t^{-\frac{1}{2}(1 \pm (1-4\lambda^2)^{\frac{1}{2}})}. \tag{4.25}$$

In view of the estimate $\lambda^2 > \frac{1}{4}$ we may write $(1-4\lambda^2)^{\frac{1}{2}} = ib$, b real, and then obtain the two independent solutions for the differential equation (4.23) in the form

$$t^{-\frac{1}{2}} t^{\mp ib} = t^{-\frac{1}{2}} \exp(\mp ib \ln t), \tag{4.26}$$

or when combining real and imaginary parts accordingly

$$\left.\begin{aligned} T_{(1)}(t) &= t^{-\frac{1}{2}} \sin(|1-4\lambda^2|^{\frac{1}{2}} \ln t), \\ T_{(2)}(t) &= t^{-\frac{1}{2}} \cos(|1-4\lambda^2|^{\frac{1}{2}} \ln t). \end{aligned}\right\} \tag{4.27}$$

Both solutions die out as $t \to \infty$, proving stability of the restricted perturbation to any initial perturbation in $\hat{u}$ or $\hat{h}$.

The analysis of the linear stability of the parabolic-cap and the M-wave solutions

becomes much more difficult when the spread g is also perturbed. We have made attempts to investigate this more general case but were essentially unsuccessful in reaching convincing conclusions. The eigenvalue problems corresponding to (4.3) and (4.19) no longer permit separable solutions. This prevented us from making exact deductions.

Nevertheless, while the above analysis is not conclusive with regard to the asymptotic behaviour of the profile starting from an arbitrary initial shape, it is still a useful one as it demonstrates stability of the parabolic-cap and the M-wave solutions to a fairly large class of perturbations. It gives us some support to suggest that numerical schemes ought to reproduce both types of similarity solutions.

5. Numerical solutions and comparisons with experiments

The governing depth-averaged equations (2.27) for conservation of mass and linear momentum were solved numerically using finite differencing for several initial conditions and parameter values. Although these equations bear a superficial resemblance to the nonlinear shallow-water wave equations and might be expected to be fairly innocuous, their numerical integration in fact turned out to be quite troublesome. This was due to several reasons. When a pile of granular material is released from rest on a slope, often the material near the rear tends initially to move up the slope. One must be careful to use appropriate upwinding in an Eulerian finite-difference discretization to avoid numerical instabilities. Unlike the analogous water-wave problem, the material is in contact with the bed over a small portion of the bed, and the depth is zero elsewhere. The flow of a granular mass can be regarded as a moving interface and it embodies all the associated difficulties of such problems. The M-wave similarity solutions contain discontinuities in both velocity and depth at the front and rear of the granular pile; these discontinuities cause significant difficulties in finite-difference computations.

Our first computations were made using Eulerian approaches. While they were able to reproduce the M-wave analytical solutions quite well, thus giving us some initial confidence in these numerical schemes, it was subsequently found that virtually any initial profile tended to evolve into the M-wave similarity solution. Since the laboratory experiments of Huber (1980) and more recent tests of Hutter *et al.* (1988, and paper in preparation) do not show convincing evidence of such trends, we now regard these numerical results for initial conditions other than the M-wave as spurious. An alternative Lagrangian scheme was then attempted. It was found to be simple and efficient and able to accurately predict the observed experimental behaviour. Prior to describing in detail the numerical approaches and results, we give a brief description of experimental work which is used as a comparison.

5.1. *Laboratory experiments*

Laboratory experiments involving the motion of gravel released from rest on a rough inclined bed were conducted by Huber (1980). A finite mass of gravel having a prescribed standard distribution of particle diameters with a mean diameter of 2.54 cm was deposited in a triangular shaped space behind a gate on the top of a plane chute of which the inclination angle was varied. The 50 cm wide chute bottom was made of a painted plywood board; the glass sidewalls of the chute permitted photographic recording of the geometry of the gravel mass during motion. In a typical experiment the gate was suddenly opened by rotating it away from the

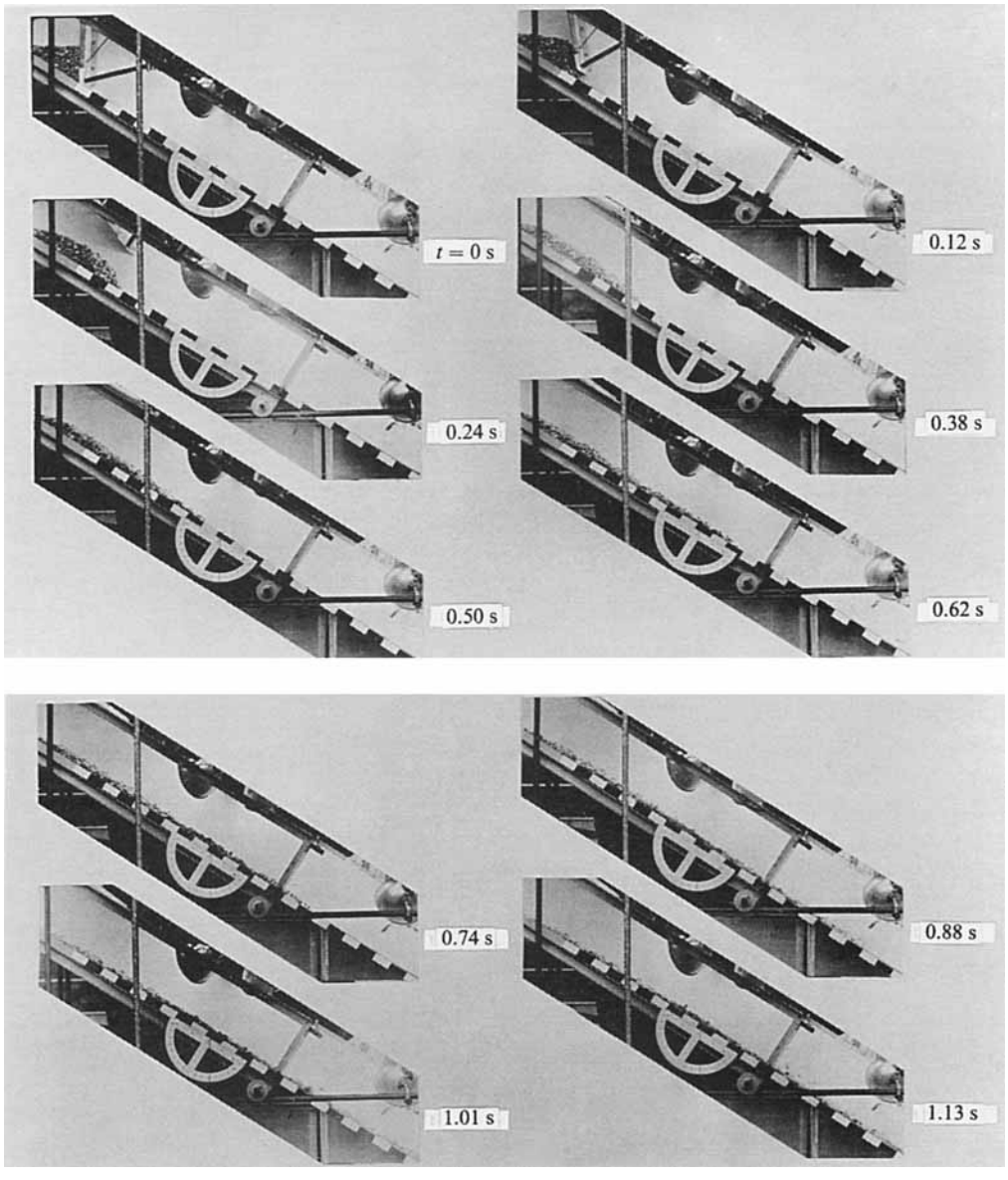

FIGURE 7. Sequence of photographs of a finite mass of gravel moving down an inclined plane taken from experiment No. 106b of A. Huber (previously unpublished). The total mass of the gravel is 80 kg, the mean diameter of the grains 2.54 cm, the inclination angle $\zeta = 32°$. Times (in s) when the photos are taken are indicated in the figure.

gravel, thereby setting the gravel in motion. Cine-films were taken at intervals of approximately 0.12 s between frames. Figure 7 shows a sequence of eleven such snapshots covering an experimental time of 1.26 s. It is seen that the gravel mass spreads quickly and approaches a long and thin layer with a depth of one of two particles after less than 1 s. The continuum approximation is certainly not satisfied for $t > 1$ s, and it may be doubtful even for $t = 0.88$ or $t = 0.714$ s.

Huber in his experiments did not record the bed friction angle δ. This was measured by us using the same plywood board and gravel with the same particle diameter distribution and it was found that $\delta \approx 22°$. These experiments were done in a quasi-static fashion by slowly increasing the angle of inclination of the plywood board and determining that angle which set the gravel mass in motion. It is known that the bed friction angles determined in this way are somewhat larger than those determined by much more difficult dynamic experiments.

Another parameter required for the theoretical comparisons is the dynamic internal friction angle. Hungr & Morgenstern (1984*b*) found in their annular-shear-cell experiments that the dynamic friction angle was about 4° less than the angle of repose of the granular material. The material used in Huber's experiment No. 106b had an angle of repose similar to that in the experiments of Hungr & Morgenstern and we have therefore used a value for ϕ of 29° in the computations described in the subsequent sections.

5.2. *Eulerian approach*

Several implicit and explicit schemes were attempted with varying degrees of apparent success. The 'upwind flux correction method' proposed by McDonald & Ambrosiano (1984) to treat flow discontinuities in hyperbolic systems was one of the more trouble-free approaches. However, the method that appeared to work the best of those attempted and the one to be described here is an adaptation of MacCormack's (1978) two-step explicit finite-difference scheme. In the first step of the approach one predicts from the known solution at time $t = n\Delta t$, the values of h and u at the new time $t = (n+1)\Delta t$ by using one-sided (upwind) differences to approximate the first derivatives. In the second step, corrections are made to the predicted values using opposite one-sided differences for the first derivatives. The method is second-order accurate and stable for appropriate time steps.

To further dampen the dispersive ripples that develop near sharp gradients we have introduced an artificial viscosity μ in both the mass and linear momentum equations used to determine h and u (see, for example, Hyman 1976, p. 69).

For the first step the finite-difference forms of the predictions for h and u at the new time step are

$$\overline{h_i^{n+1}} = h_i^n - \frac{\Delta t}{2\Delta x}(u_{i+1}^n h_{i+1}^n - u_{i-1}^n h_{i-1}^n) + \mu\frac{\Delta t}{\Delta x^2}(h_{i+1}^n - 2h_i^n + h_{i-1}^n), \tag{5.1}$$

$$\begin{aligned}\overline{u_{i+1}^{n+1}} = u_i^n &- \frac{\Delta t}{2\Delta x}u_i^n[(1-\operatorname{sgn}(u_i^n))(u_{i+1}^n - u_i^n) + (1+\operatorname{sgn}(u_i^n))(u_i^n - u_{i-1}^n)] \\ &+ \Delta t(S - \operatorname{sgn}(u_i^n)TC) - \frac{\beta}{2}\frac{\Delta t}{\Delta x}(h_{i+1}^n - h_{i-1}^n) \\ &+ \mu\frac{\Delta t}{\Delta x^2}(u_{i+1}^n - 2u_i^n + u_{i-1}^n),\end{aligned} \tag{5.2}$$

where $S = \sin\zeta$, $TC = \tan\delta\cos\zeta$, $\beta = \epsilon k_{\text{actpass}}\cos\zeta$.

In the second step the corrections for h and u at the new time are given by

$$h_i^{n+1} = \frac{1}{2}\left[h_i^n + \overline{h_i^{n+1}} - \frac{\Delta t}{2\Delta x}(\overline{u_{i+1}^{n+1}}\,\overline{h_{i+1}^{n+1}} - \overline{u_{i-1}^{n+1}}\,\overline{h_{i-1}^{n+1}}) + \frac{\mu\Delta t}{\Delta x^2}(\overline{h_{i+1}^{n+1}} - 2\overline{h_i^{n+1}} + \overline{h_{i-1}^{n+1}})\right] \tag{5.3}$$

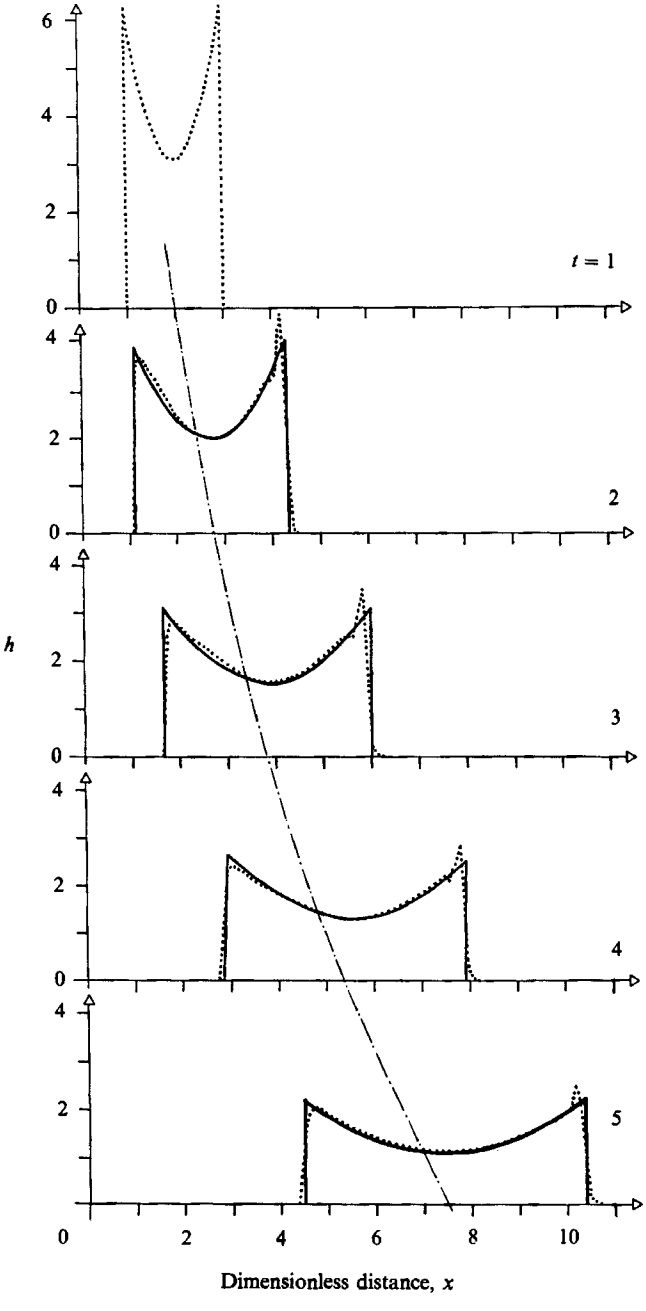

FIGURE 8. Development of M-wave with time. Comparison of analytical similarity solution with results of numerical computations using MacCormack's explicit finite-difference scheme; $\delta = 20°$, $\zeta = 45°$, $\epsilon = 0.05$, $\Delta t = 0.01$, $\Delta x = 0.05$, $\mu = 0.01$: ——, analytical solution; ....., numerical computations.

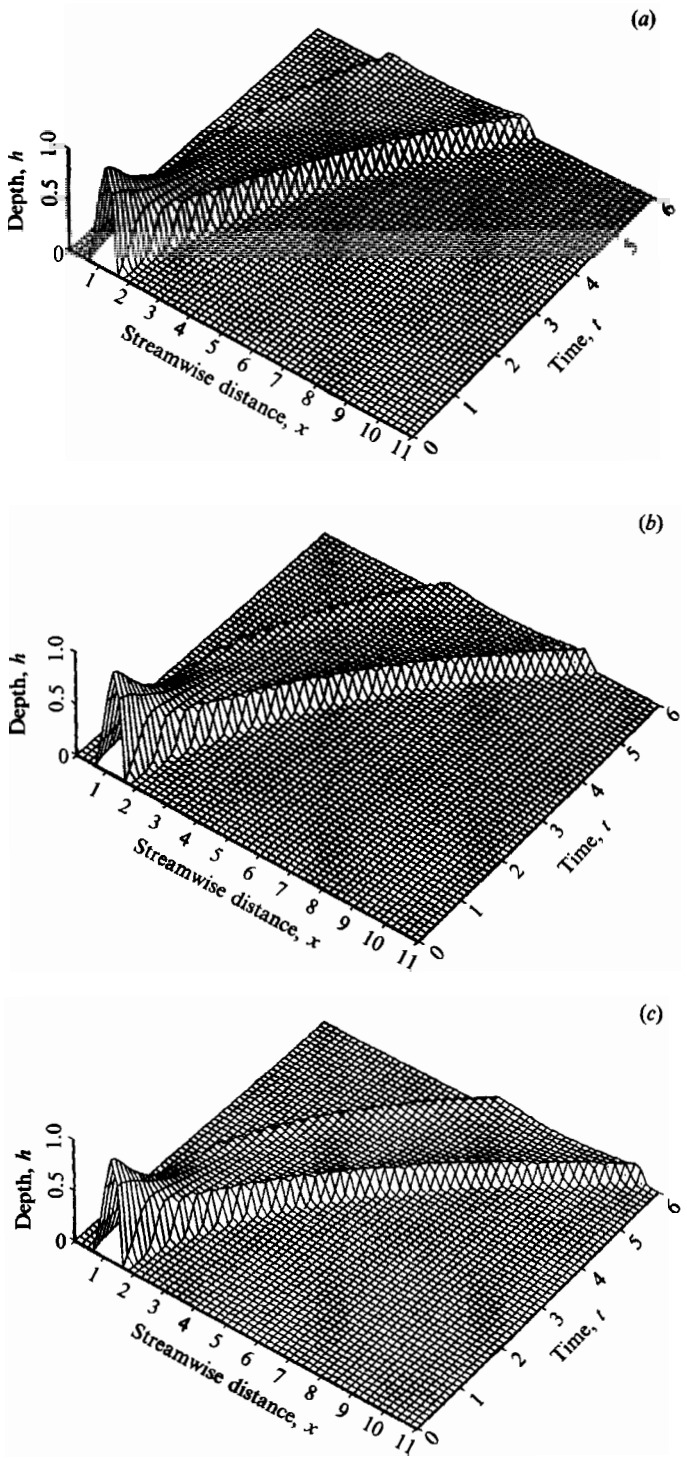

FIGURE 9. Results obtained from MacCormack's explicit Eulerian finite-difference scheme for the evolution of the motion of a finite mass of granular material starting from rest on a bed with inclination angle $\zeta = 32°$, and different bed friction angles; (*a*) $\delta = 22°$, (*b*) 16°, (*c*) 10°. $\epsilon = 0.3218$.

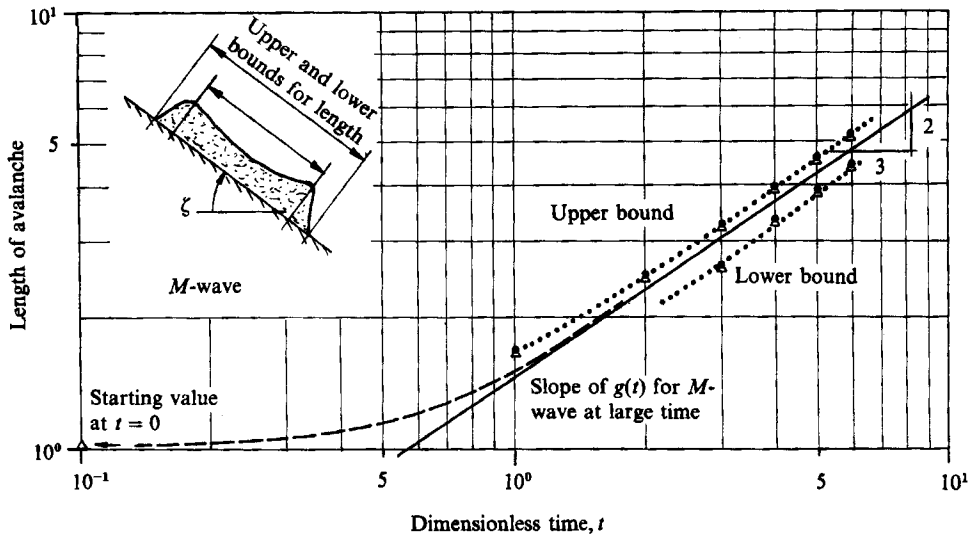

FIGURE 10. Growth of length of avalanche with time; bed slope $\zeta = 32°$, $\epsilon = 0.3218$. ⊙, $\delta = 22°$; △, $\delta = 16°$. Avalanche lengths taken from numerical calculations (Eulerian scheme) shown in figure 9.

and

$$u_i^{n+1} = \frac{1}{2}\Big[u_i^n + \overline{u_i^{n+1}} - \frac{\Delta t}{2\Delta x} u_i^{n+1}\{(1+\operatorname{sgn}(\overline{u_i^{n+1}}))(\overline{u_{i+1}^{n+1}} - \overline{u_i^{n+1}}) + (1-\operatorname{sgn}(\overline{u_i^{n+1}}))(\overline{u_i^{n+1}} - \overline{u_{i-1}^{n+1}})\}$$
$$+ \Delta t(S - \operatorname{sgn}(\overline{u_i^{n+1}})TC) - \frac{\beta}{2}\frac{\Delta t}{\Delta x}(\overline{h_{i+1}^{n+1}} - \overline{h_{i-1}^{n+1}})$$
$$+ \frac{\mu \Delta t}{\Delta x^2}(\overline{u_{i+1}^{n+1}} - 2\overline{u_i^{n+1}} + \overline{u_{i-1}^{n+1}})\Big]. \tag{5.4}$$

Values of μ of about 0.01 were found to be sufficient to keep the ripples near the 'discontinuities' small without significantly smearing out the discontinuity itself.

Figures 8–10 show some results of the numerical computations using this approach. Figure 8 displays the development of an M-wave at various non-dimensional times t. The analytical similarity solutions given by (3.25) and (3.35) were used as initial conditions for u and h at time $t = 1$ and the centre of mass of the pile was located at $x = 2$. The numerical results are compared with the similarity solution at later times. Aside from the dispersive ripples at the leading-edge discontinuity the numerical results agree well with the analytical solution. These numerical calculations were performed by taking the artificial viscosity $\mu = 0.01$; a somewhat larger value of μ eliminates the wiggles. This comparison gives some idea of the accuracy of the numerical scheme. Furthermore, the good agreement between the similarity solution and the numerical computations is in accord with the analysis of §4.2 which suggested that the M-wave solution is stable when subjected to small perturbations.

Figure 9 shows a series of calculations all at the same bed slope $\zeta = 32°$ but for different bed friction angles of 10°, 16° and 22°. As expected, decreasing the bed friction angle increases the acceleration of the pile down the slope but the rate of

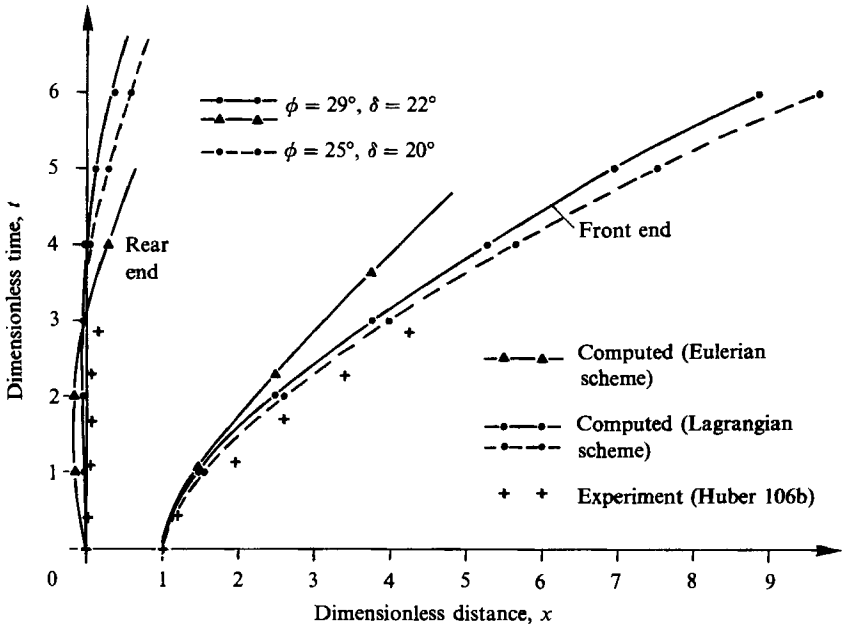

FIGURE 11. Leading and trailing edges of a gravel avalanche as they evolve in time. Experimental results are taken from A. Huber's experiments No. 106b.

spread of the length of the pile remains much the same. The granular material started from rest at time $t = 0$ with an unsymmetrical shape given by

$$\left.\begin{aligned} &\epsilon = 0.3218 \\ \text{and}\quad &h(x) = 0.879897 \sin[\pi(x-0.6)] - 0.3 \sin[2\pi(x-0.6)], \quad \text{for} \quad 0.6 < x < 1.6. \end{aligned}\right\} \tag{5.5}$$

This profile was chosen for comparison with the laboratory experiments described above and is a close approximation to the experimental depth profile of the second photograph of figure 7 and smooths the sharp corners seen in the first photographs. The initial profile is seen to evolve into the M-wave shape.

Finally, figure 10 shows the rate of growth of the length of the avalanche as its shape evolves towards the M-wave shape. At the larger times the lower bound for the length, corresponding to the distance from front to rear crests, as well as upper bound for the length, are shown. The half-length $g(t)$ from the M-wave similarity solution of §3.2 was found to grow as $t^{\frac{2}{5}}$. As may be seen, the growth rate predicted by the numerical computations as the profile approached the M-wave shape shows the same $t^{\frac{2}{5}}$ dependence.

Although it is hard to say decisively, the depth profiles from the laboratory experiments shown in figure 7 do not appear to be evolving into an M-wave shape. Furthermore, figure 11 shows that this numerical scheme gives poor predictions of the leading and trailing edges of the experimental gravel avalanche deduced from Huber's experiment No. 106b. Both these results made us question the validity of this numerical approach. After some consideration it was concluded that although the M-wave computations were correct the numerical results for more general initial profiles were spurious for the following reason.

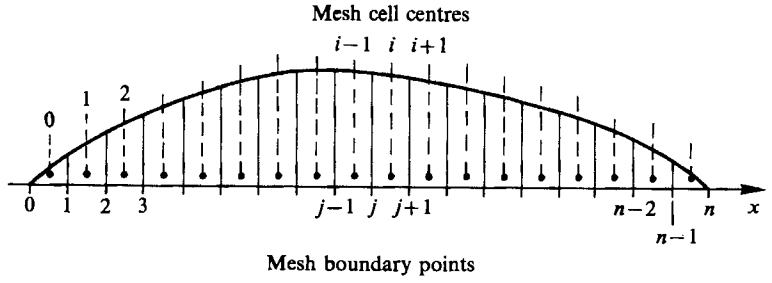

FIGURE 12. Definition of mesh cell notation for Lagrangian numerical scheme.

The Eulerian scheme made use of a fixed spatial grid which extended upstream and downstream of the moving pile. Since the pile spreads as it moves down, the nose and tail velocities are respectively higher and lower than the centre-of-mass velocity. In addition, the equations of motion (2.27) yield finite velocities upstream and downstream of the pile where there is no material and the depth is zero. Thus there occur abrupt changes in velocity corresponding to the front and rear of the pile and it was thought that these could be handled by the use of an artificial viscosity. In the numerical calculations the velocities in the regions outside of that occupied by the pile of material begin to affect (diffuse into) the region of the pile itself. This has the effect of restraining the spread of the pile and forces it to evolve towards the M-wave solution. Evidently, once it it close to that shape it continues to spread like the M-wave, as was found in figure 6. The problem is in the application of the boundary conditions. The use of the artificial viscosity which appeared to work well for the M-wave calculations has a small but cumulative effect which leads to spurious results for the evolution from initial profiles that are closer to the parabolic-cap shape. An alternative Lagrangian numerical scheme was then devised as described below.

5.3. *Lagrangian approach*

After experiencing the above-mentioned difficulties with the more commonly used Eulerian approach it was realized that a Lagrangian scheme is a more natural choice for the present problem which involves the determination of the position of the moving air–granular material interface. To formulate such an approach we divide the granular mass into a number of cells as shown on the depth profile in figure 12. The mesh cell boundaries are advected with the particles. We now set up an index notation in which i corresponds to the mesh cell centres and j corresponds to the mesh cell boundary points just to the left of i. The cell boundary points are defined at times $n-1$ and are designated as x_j^{n-1}; the velocities of the cell boundary points are defined at the half-time steps and are written as $u_j^{n-\frac{1}{2}}$.

Integrating the depth-averaged mass conservation equation, (2.27a), between x_j and x_{j+1} yields after some manipulation

$$\Delta L_i \bar{h}_i = \text{const.} \approx \Delta L_i h_i, \tag{5.6}$$

where

$$\Delta L_i = x_{j+1} - x_j, \tag{5.7}$$

$$\Delta L_i \bar{h}_i = \int_{x_j}^{x_{j+1}} h \, dx. \tag{5.8}$$

Let us assume that we know $u_j^{n-\frac{1}{2}}$, x_j^{n-1}, and h_i^{n-1}. At time $t = 0$ we identify them with

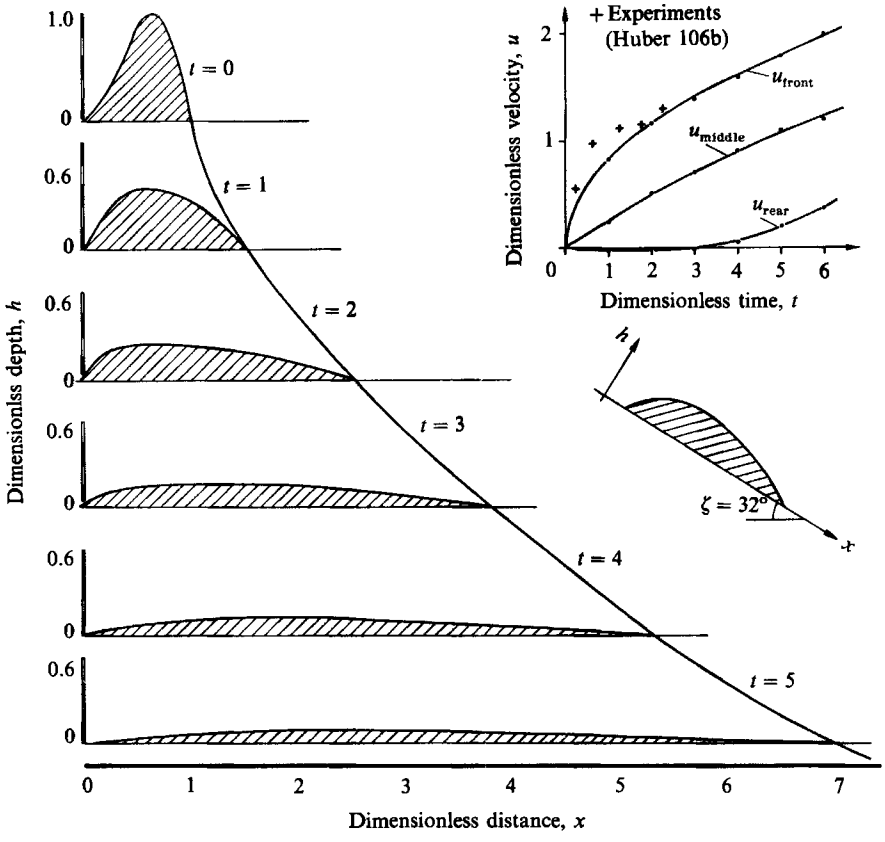

FIGURE 13. Lagrangian calcultions for avalanche profile (dimensionless x plotted against dimensionless height h) shown for six different dimensionless times. The profile tends to become more parabolic with increasing time. The inset shows the front-, middle- and rear-end velocities. Circles indicate computed values, crosses are deduced from Huber's experiment 106b. Computations were done for $\zeta = 32°$, $\phi = 29°$, $\delta = 22°$ and $\epsilon = 0.3218$.

the initial values. With these we obtain the new positions of the cell boundaries x_j^n after an elapsed time Δt, thus

$$x_j^n = x_j^{n-1} + u_j^{n-\frac{1}{2}} \Delta t. \tag{5.9}$$

We then determine the depth at the cell centres i using (5.6) and (5.7); thus

$$h_i^n = h_i^{n-1} \frac{(x_{j+1}^{n-1} - x_j^{n-1})}{(x_{j+1}^n - x_j^n)}. \tag{5.10}$$

Finally we solve for the velocities at the cell boundaries using the depth-averaged momentum equation (2.27b)

$$u_j^{n+\frac{1}{2}} = u_j^{n-\frac{1}{2}} + \Delta t \left[\sin\zeta - \cos\zeta \tan\delta \operatorname{sgn}(u_j^{n-\frac{1}{2}}) - \epsilon k_{\text{actpass}} \cos\zeta \frac{(h_i^n - h_{i-1}^n)}{(x_i^n - x_{i-1}^n)} \right], \tag{5.11}$$

where

$$x_i^n = \tfrac{1}{2}(x_j^n + x_{j+1}^n). \tag{5.12}$$

For the calculation of points other than the leading- and trailing-edge endpoints we have added an artificial viscosity term $\mu \partial^2 u / \partial x^2$ to the right-hand side of (5.11)

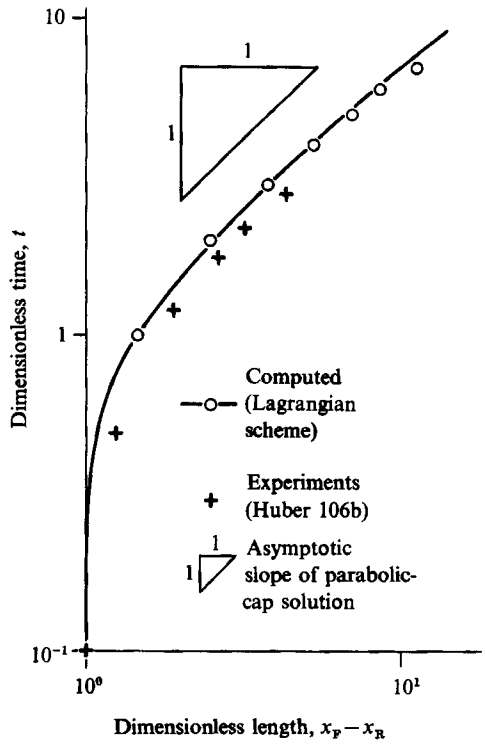

FIGURE 14. Growth of length of avalanche with time. Computations were done using Lagrangian scheme for $\zeta = 32°$, $\phi = 29°$, $\delta = 22°$ and $\epsilon = 0.3218$. Experimental points are taken from A. Huber's data for experiment No. 106b.

to dampen the numerical ripples that tend to develop under some conditions. Values for the artificial viscosity μ of between 0.01 and 0.03 proved to be adequate.

Predictions of Huber's experiment No. 106b using the Lagrangian scheme are shown in figures 11, 13, and 14. They are based upon the initial depth profile given by (5.5), zero depths at the front and rear margins, the measured, quasi-static bed friction angle $\delta = 22°$ and the estimated dynamic internal friction angle $\phi = 29°$. Figure 13 shows the profile shape at six different (dimensionless) times and as an inset the front, middle point and rear end velocities. Full and open circles mark computed values, crosses are deduced from Huber's experiments. Unfortunately these do not cover the entire range of the computed values.

It may be seen in figure 11 that the predicted position of the front is slightly behind the experimental values. For comparison we have also shown in figure 11 the results of calculations for slightly lower friction angles of $\delta = 20°$ and $\phi = 25°$ to account for a dynamic bed friction angle lower than the measured quasi-static value and for the uncertainty in the value of the internal friction angle that was not measured. The agreement is seen to be slightly better. However, it should be noted that the gravel layer was only a few particles deep at the later times in the experiments. The continuum assumption is not accurate in such instances and it is likely that individual particles rolled along the bed and over each other instead of behaving as a Coulomb continuum. In this regard we mention that extensions of the present analysis for flows down curved beds shows very good agreement with more recent experiments of Hutter, *et al.* (1988) using relatively finer particles for which the continuum approximation is more appropriate.

Last, we have plotted in figure 14 on doubly logarithmic scales the dimensionless avalanche length against dimensionless time. Experimental and computational results again match reasonably well. Computations corroborate the asymptotic parabolic-cap similarity solution behaviour (corresponding to a slope of 45°) sufficiently accurately and the experimental points indicate that this asymptotic behaviour is the one that is approached.

Given the above uncertainties paired with the inaccuracies in the definition of basal geometries and roughness one always has to accept in the geophysical context, we regard our model equations as suitable for the prediction of motion of a finite mass of a granular material subject to gravity forces. Its application to curved beds that merge into a horizontal plane will yield information regarding the travelling distance and the final spread of avalanches in their runout zones.

6. Concluding remarks

A mathematical model which describes the motion and the spreading of a finite mass of fluid-like granular material along a rough plane bed was presented. Evolution equations were derived from the balance laws of mass and momentum by depth averaging these equations. They constitute nonlinear partial differential equations for the height and the transversely averaged streamwise velocity distributions of the finite gravel mass. Two similarity solutions of these equations, a parabolic cap and an M-wave, were found; each has a different asymptotic behaviour for large time. A linear small-amplitude perturbation analysis and numerical finite-difference computations indicate that the large-time evolution of any finite mass of gravel starting from a state of rest and moving down an inclined plane tends to approach the parabolic-cap behaviour. Comparison of numerically predicted motions of a finite granular mass with laboratory experiments of rockslides showed good qualitative and fair quantitative agreement of the propagation of the front and rear margins of the avalanche as well as the evolution of the shape of the depth profile. Considerable difficulties were experienced in the development of a reliable numerical approach to integrate the depth-averaged equations of motion. While Eulerian schemes based upon MacCormack's (1978) method were able to accurately reproduce the M-wave similarity solution they gave unreliable results for more general initial conditions. A Lagrangian approach in which the computational grid was advected with the material was found to be the most simple, efficient, and reliable of the schemes attempted.

By depth averaging the equations of motion we have achieved very significant simplifications, but at the expense of losing many of the details of the flow field. The strongly fluidized, high shear rate, lower density basal layer is smeared out. One might consider an extension of the present work involving a detailed analysis that accounts for individual particle interactions, and variations of bulk density, granular temperature, etc. For such an analysis the bed boundary conditions are more numerous and much more complicated. While one anticipates variations in the ratio of shear to normal stress with variations in normal stress, density, etc. one also expects from the experimental evidence that they would at most be second-order effects.

Finally, we note that our model is suitable not only for rockfalls, landslides and sturzstroms but may equally be used also for snow avalanches if these do not develop into powder snow avalanches. The theory of such so-called flow avalanches is due to Voellmy (1955) and Salm (1966, 1968) and is based largely on hydraulics concepts;

however, we know of no computational model that could have been applied to a finite mass of snow. Our model is a first step towards a more complete analysis of these flows. Besides the application to curved beds which we regard as our next step of confirmation (Savage & Hutter 1988 and Hutter, Plüss & Savage, in preparation) these models would have to incorporate snow entrainment from below.

The contribution of S. B. Savage to this work was supported by a Natural Sciences and Engineering Research Council of Canada (NSERC) operating grant. Part of the work of S. B. Savage was completed during visits to the Laboratory of Hydraulics, Hydrology and Glaciology (VAW), ETH. He is indebted to the Director, Professor D. Vischer for financial support and for the pleasant and stimulating surroundings that made this work possible. K. Hutter is grateful for financial assistance from NSERC to visit McGill University.

We thank Dr A. Huber for making available to us his experimental results on rockslide motion and for letting us use them in this work.

REFERENCES

ABRAMOWITZ, M. & STEGUN, I. A. 1964 *Handbook of Mathematical Functions, with Formulas, Graphs and Mathematical Tables.* Dover.

ALEAN, J. 1984 Untersuchungen über Entstehungsbedingungen und Reichweiten von Eislawinen. *Mitteilung No. 74 der Versuchsanstalt für Wasserbau, Hydrologie und Glaziologie an der ETH*, pp. 1–217.

ALEAN, J. 1985 Ice avalanche activity and mass balance of a high altitude hanging glacier in the Swiss Alps. *Ann. Glaciol.* **6**, 248–249.

AUGENSTEIN, D. A. & HOGG, R. 1978 An experimental study of the flow of dry powders over inclined surfaces. *Powder Technol.* **19**, 205–215.

BAILARD, J. 1978 An experimental study of granular-fluid flow. Ph.D. dissertation, University of California, San Diego.

BRIDGWATER, J. 1972 Stress–velocity relationships for particulate solids. *ASME Paper* 72-MH-21. 7 pp.

BUGGISCH, H. & STADLER, R. 1986 On the relation between shear rate and stresses in one-dimensional steady flow of moist bulk solids. *Proc. World Congress Particle Technology, Part III. Mechanics of Pneumatic and Hydraulic Conveying and Mixing, Nürnberg, 16–18 April 1986*, pp. 187–202.

CAMPBELL, C. S. & GONG, A. 1986 The stress tensor in a two-dimensional granular shear flow. *J. Fluid Mech.* **164**, 107–125.

DAVIES, T. R. H. 1982 Spreading of rock avalanche debris by mechanical fluidization. *Rock Mech.* **15**, 9–29.

DENT, J. D. 1986 Flow properties of granular materials large overburden loads. *Acta Mech.* **64**, 111–122.

DWIGHT, H. B. 1968 *Tables of Integrals and Other Mathematical Data.* Macmillan.

ERISMANN, T. 1986 Flowing, rolling, bouncing, sliding: Synopsis of basic mechanisms. *Acta Mech.* **64**, 101–110.

FOWLER, A. C. 1980 Waves on glaciers. *J. Fluid Mech.* **140**, 283–321.

GOGUEL, J. 1978 Scale dependent rockslide mechanisms. In *Rockslides and Avalanches*, Vol. 1 (ed. B. Voight), pp. 167–180. Elsevier.

GUBLER, H.-U. 1987 Measurements and modelling of snow avalanche speeds. In *Avalanche Formation, Movement and Effects, IAHS Publ.* 126 (ed. B. Salm & H.-U. Gubler), pp. 405–420.

HAFF, P. K. 1983 Grain flow as a fluid-mechanical phenomenon. *J. Fluid Mech.* **134**, 401–430.

HANES, D. M. & INMAN, D. L. 1985 Observations of rapidly flowing granular-fluid mixtures. *J. Fluid Mech.* **150**, 357–380.

HEIM, A. 1882 Der Bergsturz von Elm. *Deutsch Geol. Gesell. Zeitschrift* **34**, 74–115.

HEIM, A. 1932 Bergsturz und Menscheleben. *Beiblatt zur Vierteljahresschrift der Natf. Ges. Zürich* **20**, 1–218.

HSÜ, K. 1975 On sturzstorms – catastrophic debris streams generated by rockfalls. *Geol. Soc. Am. Bull.* **86**, 129–140.

HSÜ, K. 1978 Albert Heim: Observations on landslides and relevance to modern interpretations. In *Rockslides and Avalanches*, Vol. 1 (ed. B. Voight), pp. 69–93. Elsevier.

HUBER, A. 1980 Schwallwellen in Seen als Folge von Felsstürzen. *Mitteilung No. 47 der Versuchsanstalt für Wasserbau, Hydrologie und Glaziologie an der ETH*, pp. 1–122.

HUNGR, O. & MORGENSTERN, N. R. 1984*a* Experiments on the flow behaviour of granular materials at high velocity in an open channel flow. *Géotechnique* **34**, 405–413.

HUNGR, O. & MORGENSTERN, N. R. 1984*b* High velocity ring shear tests on sand. *Géotechnique* **34**, 415–421.

HUTTER, K., PLÜSS, CH. & MAENO, N. 1988 Some implications deduced from laboratory experiments on granular avalanches. *Mitteilung No. 94 der Versuchsanstalt für Wasserbau, Hydrologie und Glaziologie an der ETH*, pp. 323–344.

HUTTER, K. & SAVAGE, S. B. 1988 Avalanche dynamics: The motion of a finite mass of gravel down a mountain side. *Proc. 5th Intl Symp. on Landslides, July 7–9, Lausanne, Switzerland.* 7 pp.

HUTTER, K., SZIDAROVSZKY, F. & YAKOWITZ, S. 1986 Plane steady shear flow of a cohesionless granular material down an inclined plane. A model for flow avalanches. Part II: Numerical results. *Acta Mech.* **63**, 87–112.

HYMAN, J. M. 1976 The method of lines solution of partial differential equations. *ERDA Mathematics and Computing Laboratory Rep.* C00-3077-139. Courant Institute of Mathematical Sciences, N.Y.U.

ISHIDA, M., HATANO, H. & SHIRAI, T. 1980 The flow of solid particles in an aerated inclined channel. *Powder Technol.* **27**, 7–12.

JENKINS, J. T. & RICHMAN, M. W. 1985 Grad's 13-moment system for a dense gas of inelastic spheres. *Arch. Rat. Mech. Anal.* **87**, 355–377.

JENKINS, J. T. & SAVAGE, S. B. 1983 A theory for the rapid flow of identical, smooth, nearly elastic particles. *J. Fluid Mech.* **130**, 186–202.

JOHNSON, P. C. & JACKSON, R. 1987 Frictional–collisional constitutive relations for granular materials, with application to plane shearing. *J. Fluid Mech.* **176**, 67–93.

KENT, P. E. 1965 The transport mechanism in catastrophic rockfalls. *J. Geol.* **74**, 79–83.

KNIGHT, P. C. 1983 The role of particle collisions in determining high strain rate flow behaviour. *Proc. Intl. Symp. on the Role of Particle Interactions in Powder Mech. Eindhoven*, pp. 172–182.

LUN, C. K. K., SAVAGE, S. B., JEFFREY, D. J. & CHEPURNIY, N. 1984 Kinetic theories for granular flow: inelastic particles in Couette flow and slightly inelastic particles in a general flow field. *J. Fluid Mech.* **140**, 223–256.

MACCORMACK, R. W. 1978 An efficient explicit-implicit characteristic method for solving the compressible Navier-Stokes equations. *SIAM-AMS Proc.* **11**, 130–155.

MCDONALD, B. E. & AMBROSIANO, J. 1984 High-order upwind flux correction methods for hyperbolic conservation laws. *J. Comp. Phys.* **56**, 448–460.

MCSAVENEY, M. J. 1978 Sherman Glacier rock avalanche, Alaska, U.S.A. In *Rockslides and Avalanches*, Vol. 1 (ed. B. Voight), pp. 197–258. Elsevier.

MELOSH, J. 1986 The physics of very large landslides. *Acta Mech.* **64**, 89–99.

NOREM, H., IRGENS, F. & SCHIELDROP, B. 1987 A continuum model for calculating snow avalanches. In *Avalanche Formation, Movement and Effects. IAHS Publ.* 126 (ed. B. Salm & H. Gubler), pp. 363–379.

NOVOSAD, J. 1964 Studies on granular materials. II. Apparatus for measuring the dynamic angle of internal and external friction of granular materials. *Collection Czechoslov. Chem. Commun.* **29**, No. 2697.

PERLA, I. P. & MARTINELLI, M. 1978 *Avalanche Handbook*, p. 489. US Department of Agriculture Forest Service, Agriculture Handbook.

PLÜSS, CH. 1987 Experiments on granular avalanches. Diplomarbeit, Abt X, Eidg. Techn. Hochschule, Zürich. 113 pp.

ROETHLISBERGER, H. 1974 Möglichkeiten und Grenzen der Gletscherüberwachung. *Neue Zürcher Zeitung* (Beilage: Aus Forschung und Technik) **196**, 29.

ROETHLISHBERGER, H. 1978 Eislawinen und Ausbrüche von Gletscherseen. *Jahrbuch der Schweiz. Natf. Ges. Wissenschaftl. Teil.* 170–212.

ROETHLISBERGER, H. 1981 Destructive power of glaciers. In: *Switzerland and her Glaciers, from the Ice Age to the Present*, pp. 128–165. Kümmerli & Frey, Publ. Swiss National Trust office.

ROSCOE, K. H. 1970 The influence of strain in soil mechanics. *Géotechnique* **20**, 129–170.

SALM, B. 1966 Contribution to avalanche dynamics. *IUGG/IAHS Symposium on Scientific Aspects of Snow Avalanches, Davos, Switzerland. IAHS Publ.* 69, pp. 199–214.

SALM, B. 1968 On nonuniform steady flow of avalanching snow. *IUGG/IAHS General Assembly Berne, Switzerland. IAHS Publ.* 79, pp. 19–29.

SAVAGE, S. B. 1979 Gravity flow of cohesionless granular materials in chutes and channels. *J. Fluid Mech.* **92**, 53–96.

SAVAGE, S. B. 1983 Granular flows down rough inclines – review and extension. In *Mechanics of Granular Materials: New Models and Constitutive Relations* (ed J. T. Jenkins & M. Satake), pp. 261–82. Elsevier.

SAVAGE, S. B. 1984 The mechanics of rapid granular flows. *Advances in Applied Mechanics*, Vol. 24 (ed T. Y Wu & J. Hutchinson), pp. 289–366. Academic.

SAVAGE, S. B. & SAYED, M. 1984 Stresses developed by dry cohesionless granular materials sheared in an annular shear cell. *J. Fluid Mech.* **142**, 391–430.

SCHEIDEGGER, A. E. 1975 *Physical Aspects of Natural Catastrophes.* Elsevier.

SHREVE, R. L. 1966 Sherman landslide, Alaska. *Science* **154**, 1639–1643.

SHREVE, R. L. 1968*a* Leakage and fluidization in air-lubricated avalanches. *Geol. Soc. Am. Bull.* **79**, 653–658.

SHREVE, R. L. 1968*b* The Blackhawk landslide. *Geol. Soc. Am., Spec. Paper* **108**. 47 pp.

STADLER, R. 1986 Stationäres, schnelles Fliessen von dicht gepackten trockenen und feuchten Schüttgütern. Dr.-Ing. dissertation, University of Karlsruhe, West Germany.

STADLER, R. & BUGGISCH, H. 1985 Influence of the deformation rate on shear stress in bulk solids, theoretical aspects and experimental results. *EFCE Publication Series No. 49, Reliable Flow of Particulate Solids, Proc.* Bergen, Norway, pp. 15.

STOKER, J. J. 1957 *Water Waves, the Mathematical Theory with Applications.* Interscience.

SZIDAROVSZKY, F., HUTTER, K. & YAKOWITZ, S. 1987 A numerical procedure for solving steady plane granular chute flows. *Intl. J. Num. Methods in Engng* **24**, 1993–2015.

VOELLMY, A. 1955 Über die Zerstörungskraft von Lawinen. *Schweizerische Bauzeitung* **73**, 159–162, 212–217, 246–249, 280–285.

WALTON, O. R. & BRAUN, R. L. 1986 Stress calculations for assemblies of inelastic spheres in uniform shear. *Acta Mech.* **63**, 73–86.